ACS APPLIED MATERIALS & INTERFACES

www.acsami.org

Research Article

NiFe-Layered Double Hydroxide Synchronously Activated by Heterojunctions and Vacancies for the Oxygen Evolution Reaction

Yang Luo, Yinghong Wu, Donghai Wu, Chao Huang, Dezhi Xiao, Houyang Chen,* Shili Zheng,* and Paul K. Chu*

Cite This: *ACS Appl. Mater. Interfaces* 2020, 12, 42850–42858

Read Online

ACCESS | Metrics & More | Article Recommendations | Supporting Information

ABSTRACT: The development of earth-abundant transition-metal-based electrocatalysts with bifunctional properties (oxygen evolution reaction (OER) and hydrogen evolution reaction (HER)) is crucial to commercial hydrogen production. In this work, layered double hydroxide (LDH)-zinc oxide (ZnO) heterostructures and oxygen vacancies are constructed synchronously by plasma magnetron sputtering of NiFe-LDH. Using the optimal conditions, ZnO nanoparticles are uniformly distributed on the NiFe-LDH nanoflowers, which are prepared uniformly on the three-dimensional porous Ni foam. In the LDH-ZnO heterostructures and oxygen vacancies, electrons are depleted at the Ni cations on the NiFe-LDH surface and the active sites change from Fe cations to Ni cations during OER. Our theoretical assessment confirms the change of active sites after the deposition of ZnO and reveals the charge-transfer mechanism. Owing to the significant improvement in the OER dynamics, overall water splitting can be achieved at only 1.603 V in 1 M KOH when the Ni/LDH-ZnO and Ni/LDH are used as the anode and cathode, respectively. The work reveals a novel design of self-supported catalytic electrodes for efficient water splitting and also provides insights into the surface modification of catalytic materials.

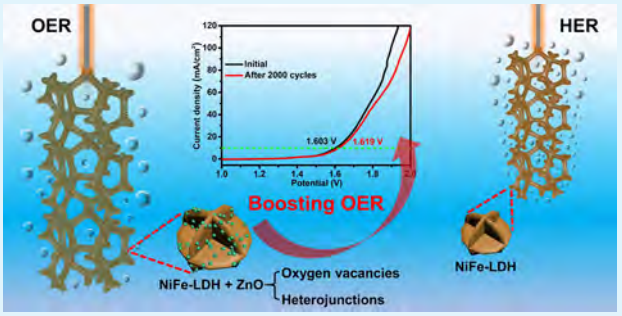

KEYWORDS: *water splitting, layered double hydroxide, plasma magnetron sputtering, heterojunctions, oxygen vacancies*

1. INTRODUCTION

The energy demand by modern society is mainly satisfied by fossil fuels and rising due to the increasing population and continuous economic development. Owing to the environmental concerns about fossil fuels, renewable energy such as solar and wind energy has gained increasing attention. Although there are a number of techniques to convert them into electrical energy, the storage of electrical energy is important for clean energy. Batteries are suitable for short-term storage of electricity but not long-term due to the inevitable self-discharging processes,[1,2] and hydrogen formation by water splitting powered by solar/wind-derived electricity is an alternative.[3,4]

Overall, water splitting contains two reactions: oxygen evolution reaction (OER) and hydrogen evolution reaction (HER). The current state-of-the-art electrocatalysts for water splitting are noble metals and noble metallic oxides such as IrO_2 for OER and Pt for HER.[5] However, because of the scarcity and long-term catalytic instability of these catalysts, the development of comparable, abundant, and stable catalysts has become a research focus.[6,7] Transition-metal oxides[8] and hydroxides[9] are alternative catalysts for OER and transition-metal sulfides,[10] carbides,[11] selenides,[12] and phosphides[13] for HER. However, most OER catalysts function in alkaline media but HER catalysts work in acidic media.[14,15] It remains a challenge for overall water splitting because of the mismatch of the working electrolytes for OER and HER as well as rising manufacturing cost for different catalytic electrodes.[16,17] Hence, the development of bifunctional catalytic electrodes for both OER and HER is needed but challenging.

Layered double hydroxides (LDHs) such as NiFe-LDH are promising bifunctional catalysts for overall water splitting in alkaline media.[16,18−21] Compared to HER, the kinetics of OER is more sluggish because of the more complex multistep electron transfer.[20,21] Acceleration of OER kinetics is crucial to the reduction of energy consumption in overall water splitting, and there is room for improvement of the OER catalytic activity of NiFe-LDHs. Techniques such as materials compounding,[22−25] surface deposition,[26−30] and surface vacancy introduction[31−33] have been proposed, but these

Received: June 30, 2020
Accepted: August 31, 2020
Published: August 31, 2020

https://dx.doi.org/10.1021/acsami.0c11847
ACS Appl. Mater. Interfaces 2020, 12, 42850−42858

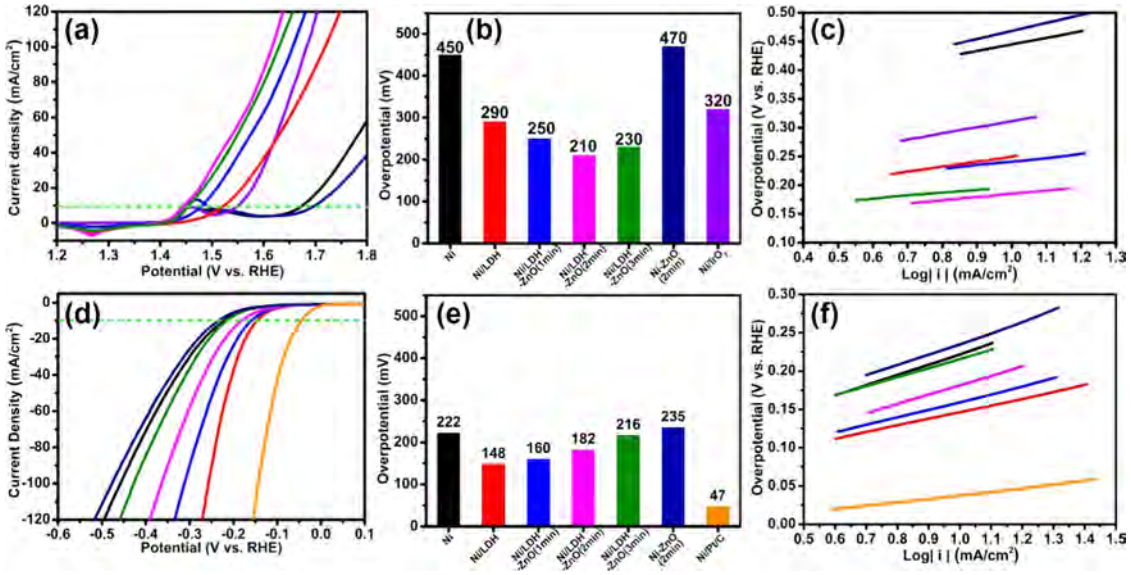

Figure 1. Electrochemical characterization: (a) OER polarization curves, (b) OER overpotentials, (c) OER Tafel plots (black, Ni, 113 mV dec^{-1}; red, Ni/LDH, 86 mV dec^{-1}; blue, Ni/LDH-ZnO (1 min), 63 mV dec^{-1}; magenta, Ni/LDH-ZnO (2 min), 57 mV dec^{-1}; olive, Ni/LDH-ZnO (3 min), 62 mV dec^{-1}; royal, Ni−ZnO (2 min), 140 mV dec^{-1}; violet, Ni/IrO_2, 104 mV dec^{-1}), (d) HER polarization curves, (e) HER overpotentials, and (f) HER Tafel plots (black, Ni, 135 mV dec^{-1}; red, Ni/LDH, 86 mV dec^{-1}; blue, Ni/LDH-ZnO (1 min), 99 mV dec^{-1}; magenta, Ni/LDH-ZnO (2 min), 117 mV dec^{-1}; olive, Ni/LDH-ZnO (3 min), 120 mV dec^{-1}; royal, Ni−ZnO (2 min), 141 mV dec^{-1}; orange, Ni/Pt/C, 46 mV dec^{-1}).

modification strategies are difficult to carry out synchronously in one step.

Zinc oxide (ZnO) with a large band gap and exciton binding energy is widely used in photocatalysis and can be used to tailor the electronic structure of electrocatalysts as the electron acceptor or donor in electrocatalysis.[34] Herein, nickel foam loaded with hydrothermally synthesized NiFe-LDH is used as a self-supporting electrode and the LDH-ZnO heterojunctions and oxygen vacancies are prepared on Ni/LDH at the same time by plasma magnetron sputtering. The overall water splitting performance is investigated with Ni/LDH-ZnO and Ni/LDH as the anode and cathode, respectively. The intrinsic activity, active sites, and stability of the electrodes are determined. The heterojunction/vacancy-induced change of OER active sites from Fe cations to Ni cations is revealed by the quasi-real-time Raman spectra and verified by theoretical calculations, suggesting new opportunities for scaling up H_2 production.

2. EXPERIMENTAL DETAILS

2.1. Synthesis of NiFe-LDH Arrays on Ni Foam. Details on the materials are provided in the Supporting Information (SI). In brief, the Ni foam (1 × 2 cm^2) was ultrasonically rinsed in HCl (37 wt %), ultrapure water, and ethanol sequentially for 5 min. The NiFe-LDH nanosheets were synthesized *in situ* on the Ni foam by a hydrothermal method. $Ni(NO_3)_2{\cdot}6H_2O$ (0.15 g), 0.2 g of $Fe(NO_3)_3{\cdot}9H_2O$, and 0.3 g of $CO(NH_2)_2$ were dissolved in 30 mL of ultrapure water and stirred magnetically for 20 min. The solution was transferred to a 50 mL Teflon-lined stainless steel autoclave, and the cleaned Ni foam was vertically suspended on a titanium wire and immersed into the solution. The autoclave was sealed and heated at a rate of 20 °C min^{-1} to 130 °C and held for 12 h. After natural cooling, Ni/LDH was ultrasonically washed with ethanol for 3 min and dried in a vacuum chamber at 30 °C.

2.2. Plasma Magnetron Sputtering. The ZnO nanoparticles were deposited on Ni/LDH using an ATC ORION plasma sputtering system (AJA International, Inc.) equipped with a DC power supply (AJA 100/300 MM3X), as shown in Figure S4 in the SI. A high-purity ZnO (99.99%) disk with a diameter of 50 mm and a thickness of 5 mm was the target. The Ni/LDH sample was vertically suspended in the chamber in a vacuum of 1 × 10^{-4} Pa and rotated at 100 rpm for uniform deposition. Sputtering was carried out using a power of 120 W, and 99.999% pure argon gas was introduced into the chamber as the sputtering gas to maintain a pressure of 13 Pa. The sputtering time was varied from 1 to 3 min to evaluate the effects of different sputtering times, while the other parameters were kept the same. The fabrication of the self-supported catalytic electrode is schematically illustrated in Figure S5 (SI), and the nomenclatures of the different electrodes are presented in Table S2 (SI).

3. RESULTS AND DISCUSSION

3.1. Electrode Characterization. The photograph of the as-prepared self-supported electrodes is shown in Figure S6 (SI), and the OER characteristics of the self-supported catalytic electrodes are displayed in Figure 1a. As expected, *in situ* fabrication of NiFe-LDH on the Ni foam boosts the OER performance and ZnO deposition by plasma magnetron sputtering improves the OER properties. Ni/LDH-ZnO (2 min) has the best OER properties, but a longer deposition time causes deterioration. After ZnO deposition on the bare Ni foam, the OER properties do not improve and even worsen slightly, indicating that ZnO itself has almost no OER catalytic activity. Hence, the OER improvement should be attributed to the LDH-ZnO electronic interactions. To produce a current density of 10 mA cm^{-2} (a universal metric corresponding to a solar-to-fuel conversion device with 10% efficiency[35,36]), an overpotential of only 210 mV is required for Ni/LDH-ZnO (2 min) and it is much less than those for the other electrodes, as shown in Figure 1b. The electrochemical kinetics is analyzed by the Tafel plots derived from the linear sweep voltammetry (LSV) curves. Figure 1c shows that the Tafel slope of Ni/LDH-ZnO (2 min) is the smallest, suggesting the fastest electrochemical reaction kinetics. Ni/LDH-ZnO (2 min) shows a smaller Tafel slope and an overpotential of 10 mA cm^{-1} than the fiducial Ni/IrO_2 catalyst. As a cathode, Ni/

https://dx.doi.org/10.1021/acsami.0c11847
ACS Appl. Mater. Interfaces 2020, 12, 42850−42858

LDH, a precursor of Ni/LDH-ZnO (2 min), shows a larger HER polarization current density than the other electrodes, as shown in Figure 1d. The overpotentials of 10 mA cm^{-1} in Figure 1e and Tafel plots in Figure 1f indicate that Ni/LDH has better HER catalytic activity than the bare Ni foam and Ni/LDH-ZnO. Ni/LDH has good HER catalytic properties such as an overpotential of 148 mV at 10 mA cm^{-1} and a Tafel slope of 86 mV dec^{-1}, although they are still worse than those of fiducial Pt/C. The Nyquist plots generated by electrochemical impedance spectroscopy (EIS) impart information about the charge-transfer resistance at the electrode/solution interface and electrochemical kinetics. As shown in Figure S7b,d (SI), the Nyquist plots of all of the samples show a semicircular shape. The semicircle diameter represents the charge-transfer resistance during the electrochemical reaction. The slight difference between the actual curves and ideal semicircle arises from the unevenness of the porous electrode surface and adsorption layer on the electrode surface. The equivalent circuit and corresponding fitted values (Figure S7c,e in the SI) indicate that Ni/LDH-ZnO (2 min) has the smallest charge-transfer resistance of 0.87 Ω in OER, whereas Ni/LDH shows the smallest charge-transfer resistance of 0.75 Ω in HER. The results reveal that the Ni/LDH-based electrode can serve as both OER and HER catalysts under alkaline conditions.

The composition of the catalysts is listed in Table S3 (SI). The atomic ratio of Ni/Fe of NiFe-LDH is 0.78, and the amount of deposited ZnO is very small. Hence, a dispersive heterojunction can be formed without covering the original active surface of NiFe-LDH. X-ray diffraction (XRD) is performed to determine the crystal structure, and the results are exhibited in Figure S8 (SI). The three diffraction peaks at 44.3, 51.8, and 76.5° correspond to the (111), (200), and (220) planes of the Ni foam (JCPDS no. 00-070-0989), respectively, and those corresponding to the crystal planes of NiFe-LDH (JCPDS no. 00-049-0188) are observed at 11.35° (003), 22.74° (006), 34.41° (012), 38.77° (015), and 59.98° (110). After magnetron sputtering, no additional diffraction peak appears since ZnO has a small quantity and crystallinity. The peak intensity of NiFe-LDH decreases due to defects caused by plasma sputtering.[37] By comparing the diffraction patterns of Ni/LDH-ZnO, a longer sputtering time attenuates the peaks of NiFe-LDH.

The scanning electron microscopy (SEM) images of Ni/LDH and Ni/LDH-ZnO are displayed in Figure S9 (SI). Figure S9a–c reveals the dense and uniformly distributed NiFe-LDH nanoflowers on the three-dimensional (3D) porous Ni substrate. The NiFe-LDH nanoflowers have a size of 300–500 nm, and each nanoflower is composed of several ultrathin nanosheets with a size of about 200 nm. Figure S9d–l shows that the nanosheet structure of NiFe-LDH is maintained after sputtering and a shorter sputtering time gives rise to a more uniform dispersion of ZnO on NiFe-LDH. When the sputtering time is 3 min, the ZnO nanoparticles agglomerate slightly and ZnO partially covers the active sites of the NiFe-LDH substrate. This explains the relationship between the morphology and electrochemical properties. The LDH-ZnO heterojunctions promote the catalytic activity of OER, but excessive deposition causes the aggregation of ZnO, consequently hiding some of the active sites on the NiFe-LDH substrate, leading to poorer catalytic activity. The transmission electron microscopy (TEM) images show a smooth surface on original NiFe-LDH (Figure 2a) and uniform distribution of ZnO nanoparticles on NiFe-LDH after sputtering (Figure 2c).

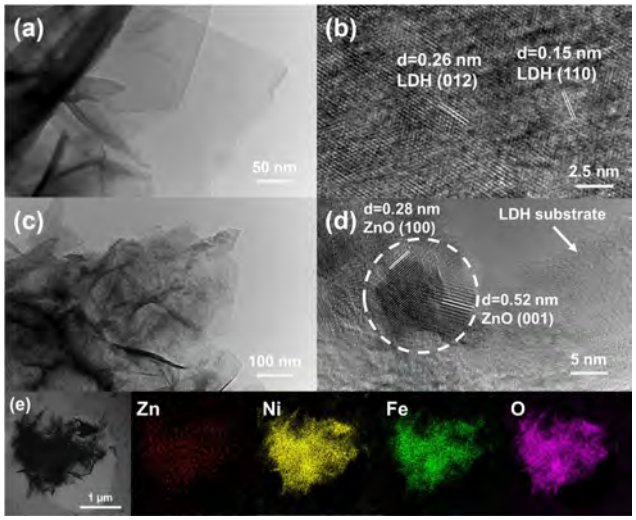

Figure 2. (a) TEM image and (b) HR-TEM image of NiFe-LDH and (c) TEM image, (d) HR-TEM image, and (e) EDS maps of LDH-ZnO (2 min).

Figure 2b shows that NiFe-LDH has interplanar spacings of 0.26 and 0.15 nm corresponding to the (012) and (110) planes of NiFe-LDH (JCPDS no. 00-049-0188).[16,26] Figure 2d indicates that the ZnO nanoparticles have a size of 10 nm and the lattice spacings of 0.28 and 0.52 nm match the (100) and (001) planes of hexagonal ZnO (JCPDS no. 00-089-1397).[34] The uniformity of the ZnO nanoparticles on the NiFe-LDH substrate is corroborated by energy-dispersive spectroscopy (EDS) mapping, as shown in Figure 2e. The agglomeration and coverage by ZnO after excessive deposition are confirmed by TEM, as shown in Figure S10 (SI). In addition, when the deposition time is long (1 h), the ZnO phase can be detected by the XRD pattern and Raman spectrum, revealing a cubic phase (JCPDS no. 00-089-1397), as shown in Figure S11 in the SI, consistent with the high-resolution TEM (HR-TEM) image.

3.2. Intrinsic Activity and Active Sites. The electrode area that actually participates in the electrochemical reaction is represented by the electrochemically active surface area (ECSA). By measuring the electrical double layer capacitor (C_{dl}), as shown in Figure S12 (SI), the ECSAs of Ni/LDH and Ni/LDH-ZnO (2 min) are calculated to be 22.9 and 27.5 cm^2, respectively. The current density normalized by ECSA reflects the intrinsic activity of the electrode, and Figure 3a,c shows that Ni/LDH-ZnO (2 min) and Ni/LDH have higher catalytic activities in OER and HER, respectively. The turnover frequency (TOF) is another key parameter to evaluate the intrinsic activity of the catalytic electrode and a larger TOF represents a higher atom utilization efficiency and faster kinetics per active site. It can be observed that Ni/LDH-ZnO (2 min) and Ni/LDH have higher intrinsic activity in OER and HER, respectively, which is in agreement with the polarization curves normalized by ECSA.

The X-ray photoelectron spectroscopy (XPS) survey spectra in Figure S13 (SI) confirm the presence of Ni, Fe, and O on the surface of Ni/LDH and Ni, Fe, Zn, and O on Ni/LDH-ZnO (2 min). The Ni 2p spectra in Figure 4a exhibit two spin–orbit peaks of Ni $2p_{1/2}$ and Ni $2p_{3/2}$ coordinated to OH and shakeup satellites. The subpeaks with lower binding energy are attributed to Ni^{2+}, and the subpeaks with higher binding energy belong to Ni^{3+}.[16,26,32,33,38] The relative increase of the

https://dx.doi.org/10.1021/acsami.0c11847
ACS Appl. Mater. Interfaces 2020, 12, 42850–42858

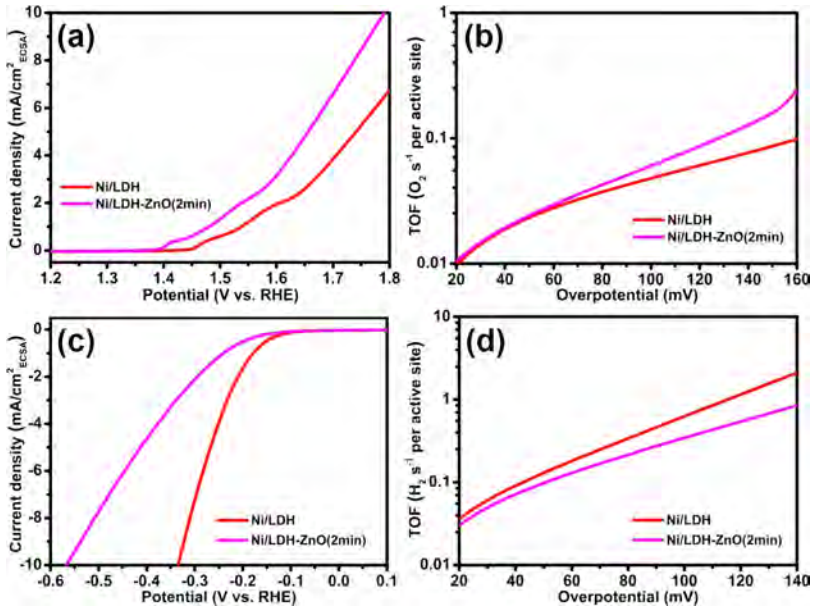

Figure 3. (a) Polarization curves normalized by ECSA for OER, (b) TOF plots with respect to the overpotential for OER, (c) polarization curves normalized by ECSA for HER, and (d) TOF plots with respect to the overpotential for HER.

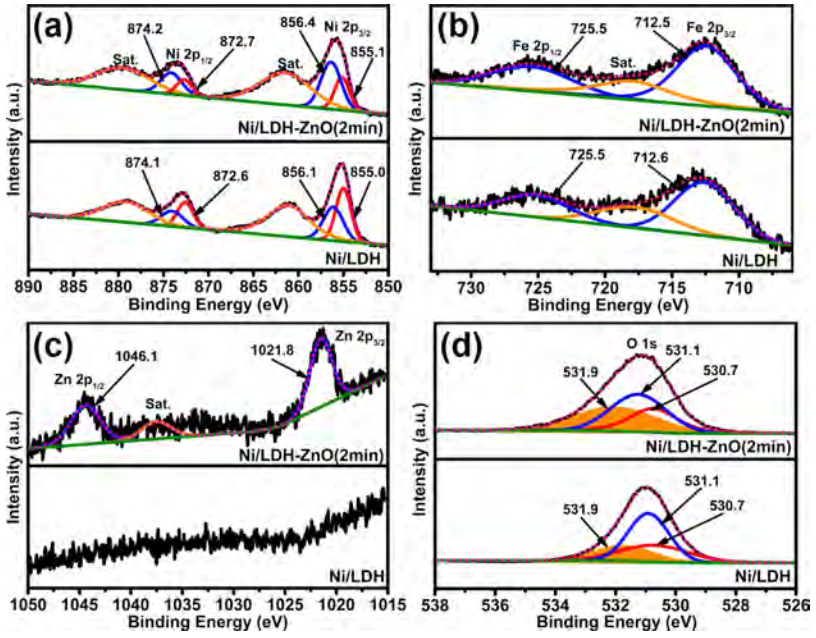

Figure 4. High-resolution XPS spectra of Ni/LDH and Ni/LDH-ZnO (2 min): (a) Ni 2p, (b) Fe 2p, (c) Zn 2p, and (d) O 1s.

subpeaks with higher binding energy as well as the concomitant broadening of Ni 2p suggests an increased concentration of Ni^{3+} from 45.3 to 66.3% in NiFe-LDH after the formation of LDH-ZnO heterojunctions. The larger amount of Ni^{3+} ($t_{2g}^{6}e_{g}^{1}$) suggests electron depletion at the Ni cations on NiFe-LDH, and occupancy of e_g orbitals of the surface Ni cations is close to unity, consequently favoring the OER reactivity.[39,40] The Fe 2p spectra in Figure 4b show Fe^{3+} coordination with OH,[16,26,32,41] and there is no obvious change in the Fe 2p peaks after ZnO deposition. It suggests that electron depletion at the Ni cations stems from deposited ZnO instead of Fe cations. As shown in Figure 4c, no Zn signal is detected from Ni/LDH and the Zn 2p peaks of Ni/LDH-ZnO (2 min) shift to a lower energy by 0.5 eV compared to those of normal ZnO. Electron accumulation can be observed from the Zn 2p spectra. As shown in Figure 4d, the change in the O 1s spectra reflects the vacancy contribution after plasma magnetron sputtering. The subpeak at 530.7 eV represents oxygen bonded with metals, that at 531.1 eV is assigned to OH groups coordinated with Fe and Ni, and that at 531.9 eV is characteristic of oxygen vacancies and defects.[32,41−43] The concentration of oxygen vacancies in Ni/LDH-ZnO (2 min) is larger than that in Ni/LDH, resulting from the local electron potential difference between NiFe-LDH and ZnO[41] as well as reduction and etching effects by the plasma.[44] The electron paramagnetic resonance (EPR) spectra in Figure S14 (SI) show that the characteristic signal of oxygen vacancies in Ni/LDH-ZnO (2 min) is more intense than that of Ni/LDH,

https://dx.doi.org/10.1021/acsami.0c11847
ACS Appl. Mater. Interfaces 2020, 12, 42850−42858

further corroborating the generation of oxygen vacancies during magnetron sputtering. As a result, electrons that originally occupied the O 2p orbitals delocalize around the metal cations to lower the adsorption energy of H_2O and increase active sites around these defects.[33,42,44−46] Previous studies have also proved that electrons excited to the conduction band enable weaker metal−oxygen bonds to yield faster exchange of electrons and intermediates, thus boosting the OER efficiency.[42,44−46] Although the deposited ZnO covers some active sites on the NiFe-LDH substrate, an increase in oxygen vacancies as new active sites offsets this effect and hence the total number of active sites increases as shown by the ECSA measurement.

To investigate the actual active phases, quasi-real-time Raman spectra are acquired at different reaction times, as shown in Figures 5 and S15 (SI). The Raman peak at 1060 cm^{-1} corresponds to intercalated carbonate in NiFe-LDH. The Raman peaks of Ni/LDH-ZnO (2 min) and Ni/LDH are almost the same because the amount of deposited ZnO is too small, and the peaks at 455 and 526 cm^{-1} are attributed to metal−oxygen vibrations for $Ni(OH)_2$[47] and γ-FeOOH[48] in NiFe-LDH, respectively. γ-FeOOH (Fe^{3+}) matches the XPS spectra of Fe 2p in Figure 4b, and it has been reported to promote the dissociation of water molecules.[16] However, the peaks of these two samples in the range between 250 and 750 cm^{-1} are very different during OER (Figure 5) and HER (Figure S15 in the SI). With regard to Ni/LDH, the Raman peak position hardly changes during OER, indicating that the Fe cations are the active sites ($FeO + H_2O \rightarrow FeO{-}OH_{ads} + e^-$). As OER proceeds, the Raman peaks of Ni/LDH-ZnO (2 min) shift to frequencies of 477 and 557 cm^{-1} characteristic of γ-NiOOH (Ni^{3+}).[49,50] The transformation of $Ni(OH)_2$ to γ-NiOOH demonstrates that the Ni cations constitute the effective active sites ($NiO + H_2O \rightarrow NiO{-}OH_{ads} + e^-$) on the surface of Ni/LDH-ZnO (2 min), and so, it can be inferred that the change in active sites is caused by the LDH-ZnO heterojunctions and oxygen vacancies.

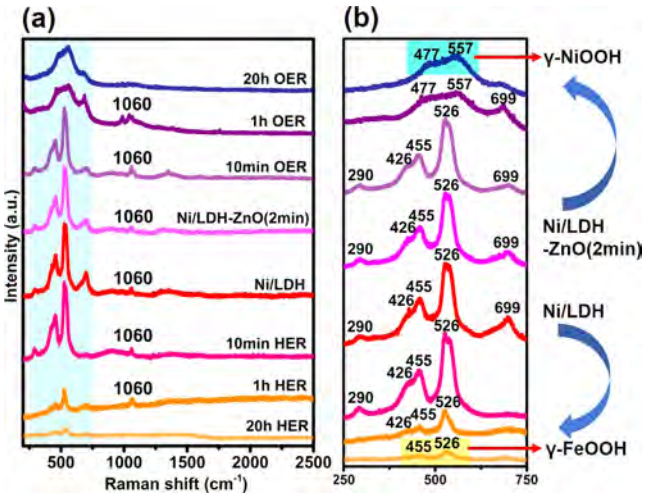

Figure 5. (a) Quasi-real-time Raman spectra under OER conditions for different times and (b) magnification of the blue region in (a).

Theoretical calculations are performed to analyze the quasi-real-time Raman results. The model is displayed in Figure S1 (SI), and the corresponding construction process is described in the SI. Since the free energy or overpotential depends on the total energy of the particular adsorption configuration, all possible adsorption configurations are taken into account, and the most stable configurations are presented in Figure S16 (SI). The density functional theory (DFT) results show that the exposed Fe or Ni sites are the preferred positions for the adsorption of the intermediates. The free energy diagrams of NiFe-LDH (Figure S17 in the SI) indicate that the overpotentials of the Ni and Fe sites on the (110) facets are 1.258 and 0.872 V, respectively. Compared to the Ni sites, the lower overpotential of the Fe sites suggests that the Fe sites are the active sites on the (110) facets (Figure S16d−f). The results are in agreement with the experimental data including the quasi-real-time Raman results. The rate-limiting step is the formation of O* at the Ni site, while it turns to the formation of OOH* at the Fe site.

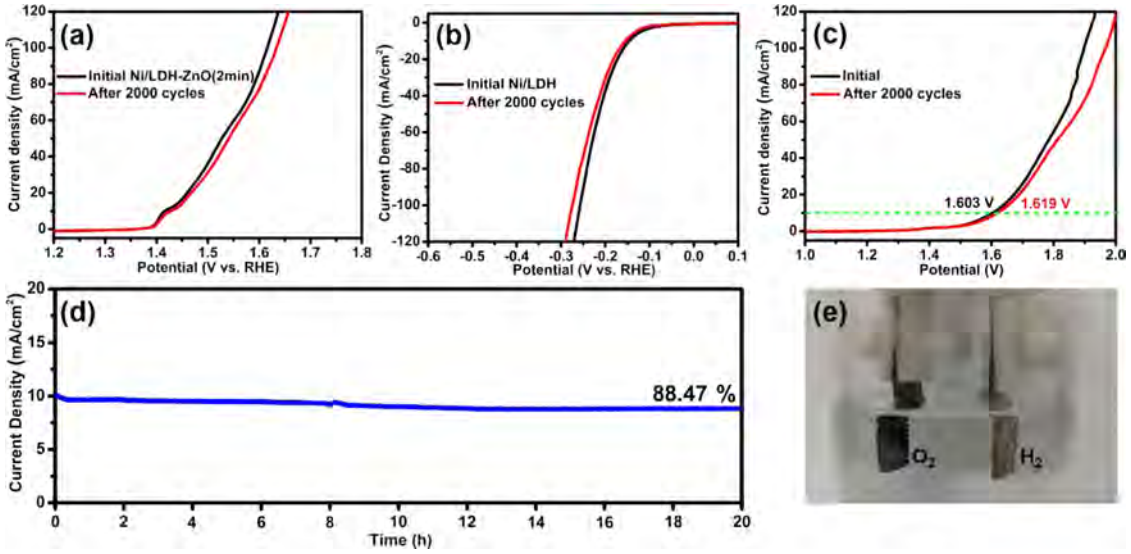

Figure 6. (a) Cycling stability of Ni/LDH-ZnO (2 min) for OER, (b) cycling stability of Ni/LDH for HER, (c) cycling stability for overall water splitting with the Ni/LDH-ZnO (2 min) | KOH (1 M) | Ni/LDH system in a two-electrode configuration, (d) time-dependent current density at 1.62 V in the two-electrode configuration, and (e) photograph of the water splitting process.

https://dx.doi.org/10.1021/acsami.0c11847
ACS Appl. Mater. Interfaces 2020, 12, 42850−42858

The OER catalytic characteristics of NiFe-LDH loaded with ZnO are determined. A simplified model, *i.e.*, the Zn-doped (110) facet of NiFe-LDH, is implemented, and the process is shown in the SI. The Zn atoms are encircled by O atoms (Figure S18 in the SI) similar to the ZnO atmosphere. According to Figures S18 and S19 (SI), the calculated overpotential (Figure S18a–c) of Ni sites on the Zn-doped system is 0.466 V, which is much lower than that of the pristine (110) facet of NiFe-LDH (1.258 V). However, the overpotential (Figure S18d–f) is 1.098 V for Fe sites on the Zn-doped system, which is higher than that on the pristine system (0.872 V). The overpotential of the Ni sites on the Zn-doped system (0.466 V) is smaller than that at Fe sites on the Zn-doped one (0.872 V), suggesting that the Ni sites are active in the OER process. In conclusion, the deposition of ZnO on NiFe-LDH lowers the OER overpotential and modifies the active sites from Fe to Ni sites on the (110) facet. The rate-limiting steps for Fe and Ni sites on the Zn-doped systems are the same as those of the pristine system.

To elucidate the mechanism governing the change of the active sites, the electronic properties (charge transfer) are investigated by the Bader charge analysis. On the pristine (110) facet (Table S4 in the SI), 0.885, 1.169, and 0.917 |e| are transferred from Ni to O atoms with adsorption of OH*, O*, and OOH* intermediates on the Ni active sites, respectively, and 1.246, 1.537, and 1.435 |e| are transferred from the Fe to O atoms with adsorption of OH*, O*, and OOH* intermediates on the Fe active site, respectively. However, by introducing ZnO to NiFe-LDH, the Ni active sites with adsorption of OH*, O*, and OOH* intermediates lose 1.08, 1.186, and 1.101 |e|, respectively, which are more than those on the pristine facet. The Fe active sites on the Zn-doped system with adsorption of OH*, O*, and OOH* intermediates lose 1.225, 1.405, and 1.42 |e|, respectively, which are less than those on the pristine facet. The electron transfer results indicate that the loading of ZnO may decrease the reactivity of Fe sites but increase the reactivity of Ni sites. Thus, with the aid of ZnO, the active sites for OER on the (110) facet change from Fe to Ni. The charge-transfer assessment is consistent with the XPS results.

3.3. Overall Water Splitting and Electrolytic Stability.

The long-term stability of the electrodes is crucial to practical applications. As shown in Figure 6a,b, Ni/LDH-ZnO (2 min) and Ni/LDH show almost no degradation after 2000 cycles under OER and HER conditions. When Ni/LDH-ZnO (2 min) and Ni/LDH are combined in the electrolytic system for overall water splitting, the two-electrode configuration has competitive catalytic properties and excellent stability (Figure 6c). Only 1.603 and 1.619 V are required to achieve a current density of 10 mA cm^{-2} initially and after 2000 cycles. As shown in Figure S20 (SI), the benchmark coupled IrO_2-Pt/C electrolyzer requires a cell voltage of 1.647 V at 10 mA cm^{-2}, which displays worse performance for water splitting. The electrocatalytic properties are summarized in Table S5 (SI) with reference to the literature, and the combination of Ni/LDH-ZnO (2 min) and Ni/LDH delivers outstanding performance. The Ni/LDH is a precursor of the Ni/LDH-ZnO (2 min) during the preparation and so the manufacturing cost can be reduced. Figure 6d shows the steady-state electrolytic curve of the two-electrode system at 1.62 V, and the current density is maintained during the operation for 20 h. Only a decrease of 11.53% is observed from the current density, confirming the good structural and chemical stability, and the robust production of O_2 and H_2 is demonstrated in Figure 6e.

To further verify the structural stability of the electrodes, SEM images are acquired after testing for 20 h, as shown in Figure S21 (SI). The structure is almost intact, although slight breakage can indeed be observed, and it explains the slight current drop in Figure S21d. The TEM images in Figure S22 (SI) confirm the structural stability of the catalysts and the substantial binding between the NiFe-LDH substrate and ZnO nanoparticles. The XRD patterns after the stability test in Figure S23 (SI) reveal that γ-NiOOH and γ-FeOOH are formed in Ni/LDH-ZnO (2 min) and Ni/LDH, respectively, in accordance with the quasi-real-time Raman spectra. The XPS spectra after the stability test in Figure S24 (SI) show almost no significant changes except an increase in Fe^{2+} and a decrease in oxygen vacancies after OER. ZnO can be stabilized due to the electron transfer in the heterostructure. Besides, the surface passivation of ZnO can be achieved by the plasma magnetron sputtering technique, resulting in an improvement in the crystallinity, stability, and electrocatalytic properties.[51] All in all, the chemical stability of the two electrodes is excellent. The yields of H_2 and O_2 show that the overall water splitting process exhibits almost 100% faradic efficiency at 10 mA cm^{-2} for 60 min, as shown in Figure S25 in the SI.

4. CONCLUSIONS

LDH-ZnO heterostructures and oxygen vacancies are constructed synchronously by plasma magnetron sputtering of NiFe-LDH prepared on Ni foam. The ZnO nanoparticles are uniformly distributed on the NiFe-LDH nanoflowers, which are prepared uniformly on the 3D porous Ni foam. NiFe-LDH and Ni/LDH-ZnO can be produced simultaneously and overall water splitting can be achieved at only 1.603 V with Ni/LDH-ZnO and Ni/LDH being the anode and cathode, respectively. The excellent characteristics can be attributed to the improvement of the rate-determining OER dynamics. Electron depletion at Ni cations caused by the LDH-ZnO heterojunctions and formation of oxygen vacancies confirmed by XPS contribute to the OER catalytic activity synergistically. In the presence of the LDH-ZnO heterojunctions and oxygen vacancies, the quasi-real-time Raman spectra demonstrate the change of active sites from Fe cations to Ni cations during OER and the DFT + *U* calculation reveals the mechanism and verifies the reliability. The results not only suggest a promising system and concept for efficient water splitting but also offer insights into the surface modification of catalytic materials.

■ ASSOCIATED CONTENT

Supporting Information

The Supporting Information is available free of charge at https://pubs.acs.org/doi/10.1021/acsami.0c11847.

Material details; electrochemical assessment and material characterization details; DFT calculation details and results; preparation of IrO_2- and Pt/C-loaded Ni foams; LSV reverse scan method; calculation of the electrochemically active surface area (ECSA) and turnover frequency (TOF); effects of the Ni/Fe ratio on the catalytic performance; plasma magnetron sputtering system; nomenclatures of the different electrodes; photographs of the samples; Nyquist plots, atomic ratios, XRD patterns, SEM images, TEM images, CV curves, XPS survey spectra, EPR spectra, and quasi-real-

https://dx.doi.org/10.1021/acsami.0c11847
ACS Appl. Mater. Interfaces 2020, 12, 42850–42858

time Raman spectra of the samples; comparison of the water splitting performance; SEM images, TEM images, XRD patterns, and XPS spectra of the samples after the stability test; and faradic efficiency in overall water splitting (PDF)

AUTHOR INFORMATION

Corresponding Authors

Houyang Chen − *Department of Chemical and Biological Engineering, University at Buffalo, The State University of New York, Buffalo, New York 14260-4200, United States*; Email: hchen23@buffalo.edu

Shili Zheng − *CAS Key Laboratory of Green Process and Engineering, National Engineering Laboratory for Hydrometallurgical Cleaner Production Technology, Institute of Process Engineering, Chinese Academy of Sciences, Beijing 100190, China*; orcid.org/0000-0001-9474-9503; Email: slzheng@ipe.ac.cn

Paul K. Chu − *Department of Physics, Department of Materials Science and Engineering, and Department of Biomedical Engineering, City University of Hong Kong, Kowloon 999077, Hong Kong SAR*; orcid.org/0000-0002-5581-4883; Email: paul.chu@cityu.edu.hk

Authors

Yang Luo − *Department of Physics, Department of Materials Science and Engineering, and Department of Biomedical Engineering, City University of Hong Kong, Kowloon 999077, Hong Kong SAR; Centre for Environmental Engineering Research, Department of Civil Engineering and Department of Mechanical Engineering, The University of Hong Kong, Pokfulam 999077, Hong Kong SAR; CAS Key Laboratory of Green Process and Engineering, National Engineering Laboratory for Hydrometallurgical Cleaner Production Technology, Institute of Process Engineering, Chinese Academy of Sciences, Beijing 100190, China*; orcid.org/0000-0003-4536-3457

Yinghong Wu − *Centre for Environmental Engineering Research, Department of Civil Engineering and Department of Mechanical Engineering, The University of Hong Kong, Pokfulam 999077, Hong Kong SAR; CAS Key Laboratory of Green Process and Engineering, National Engineering Laboratory for Hydrometallurgical Cleaner Production Technology, Institute of Process Engineering, Chinese Academy of Sciences, Beijing 100190, China; School of Energy and Environment, City University of Hong Kong, Kowloon 999077, Hong Kong SAR*

Donghai Wu − *Henan Key Laboratory of Nanocomposites and Applications, Institute of Nanostructured Functional Materials, Huanghe Science and Technology College, Zhengzhou 450006, China*

Chao Huang − *Department of Physics, Department of Materials Science and Engineering, and Department of Biomedical Engineering, City University of Hong Kong, Kowloon 999077, Hong Kong SAR*; orcid.org/0000-0003-2371-5722

Dezhi Xiao − *Department of Physics, Department of Materials Science and Engineering, and Department of Biomedical Engineering, City University of Hong Kong, Kowloon 999077, Hong Kong SAR*

Complete contact information is available at: https://pubs.acs.org/10.1021/acsami.0c11847

Notes

The authors declare no competing financial interest.

ACKNOWLEDGMENTS

The work was supported by the City University of Hong Kong Strategic Research Grant (SRG) [grant number 7005105], the Hong Kong Research Grants Council (RGC) General Research Fund (GRF) [grant number CityU 11205617], and the National Natural Science Foundation of China [grant number 51774261]. The authors thank Prof. Xiao-yan Li at The University of Hong Kong for his technological help.

REFERENCES

(1) Podder, A.; Kapner, M. *Analysis of Batteries for Use in Photovoltaic Systems. Final Report*; Hittman Associates, Inc.: Columbia, MD (USA), 1981.

(2) Seong, W. M.; Park, K.-Y.; Lee, M. H.; Moon, S.; Oh, K.; Park, H.; Lee, S.; Kang, K. Abnormal Self-Discharge in Lithium-Ion Batteries. *Energy Environ. Sci.* **2018**, *11*, 970−978.

(3) Coughlin, R. W.; Farooque, M. Hydrogen Production from Coal, Water and Electrons. *Nature* **1979**, *279*, 301−303.

(4) Carrasco, J. M.; Franquelo, L. G.; Bialasiewicz, J. T.; Galván, E.; PortilloGuisado, R. C.; Prats, M. M.; León, J. I.; Moreno-Alfonso, N. Power-Electronic Systems for the Grid Integration of Renewable Energy Sources: A Survey. *IEEE Trans. Ind. Electron.* **2006**, *53*, 1002−1016.

(5) Xing, J.; Li, H.; Cheng, M. M.-C.; Geyer, S. M.; Ng, K. S. Electro-synthesis of 3D Porous Hierarchical Ni−Fe Phosphate Film/Ni Foam as a High-Efficiency Bifunctional Electrocatalyst for Overall Water Splitting. *J. Mater. Chem. A* **2016**, *4*, 13866−13873.

(6) Wang, H.; Lee, H.-W.; Deng, Y.; Lu, Z.; Hsu, P.-C.; Liu, Y.; Lin, D.; Cui, Y. Bifunctional Non-noble Metal Oxide Nanoparticle Electrocatalysts through Lithium-Induced Conversion for Overall Water Splitting. *Nat. Commun.* **2015**, *6*, No. 7261.

(7) Alarawi, A.; Ramalingam, V.; He, J.-H. Recent Advances in Emerging Single Atom Confined Two-Dimensional Materials for Water Splitting Applications. *Mater. Today Energy* **2019**, *11*, 1−23.

(8) Hong, W. T.; Risch, M.; Stoerzinger, K. A.; Grimaud, A.; Suntivich, J.; Shao-Horn, Y. Toward the Rational Design of Non-precious Transition Metal Oxides for Oxygen Electrocatalysis. *Energy Environ. Sci.* **2015**, *8*, 1404−1427.

(9) Morales-Guio, C. G.; Liardet, L.; Hu, X. Oxidatively Electrodeposited Thin-Film Transition Metal (Oxy) Hydroxides as Oxygen Evolution Catalysts. *J. Am. Chem. Soc.* **2016**, *138*, 8946−8957.

(10) Guo, Y.; Park, T.; Yi, J. W.; Henzie, J.; Kim, J.; Wang, Z.; Jiang, B.; Bando, Y.; Sugahara, Y.; Tang, J.; Yamauchi, Y. Nanoarchitectonics for Transition-metal-sulfide-based Electrocatalysts for Water Splitting. *Adv. Mater.* **2019**, *31*, No. 1807134.

(11) Esposito, D. V.; Hunt, S. T.; Kimmel, Y. C.; Chen, J. G. A New Class of Electrocatalysts for Hydrogen Production from Water Electrolysis: Metal Monolayers Supported on Low-Cost Transition Metal Carbides. *J. Am. Chem. Soc.* **2012**, *134*, 3025−3033.

(12) Feng, W.; Pang, W.; Xu, Y.; Guo, A.; Gao, X.; Qiu, X.; Chen, W. Transition Metal Selenides for Electrocatalytic Hydrogen Evolution Reaction. *ChemElectroChem* **2020**, *7*, 31−54.

(13) Du, H.; Kong, R.-M.; Guo, X.; Qu, F.; Li, J. Recent Progress in Transition Metal Phosphides with Enhanced Electrocatalysis for Hydrogen Evolution. *Nanoscale* **2018**, *10*, 21617−21624.

(14) Gong, M.; Wang, D.-Y.; Chen, C.-C.; Hwang, B.-J.; Dai, H. A Mini Review on Nickel-Based Electrocatalysts for Alkaline Hydrogen Evolution Reaction. *Nano Res.* **2016**, *9*, 28−46.

(15) Su, J.; Yang, Y.; Xia, G.; Chen, J.; Jiang, P.; Chen, Q. Ruthenium-Cobalt Nanoalloys Encapsulated in Nitrogen-Doped Graphene as Active Electrocatalysts for Producing Hydrogen in Alkaline Media. *Nat. Commun.* **2017**, *8*, No. 14969.

(16) Qiu, Z.; Tai, C.-W.; Niklasson, G. A.; Edvinsson, T. Direct Observation of Active Catalyst Surface Phases and the Effect of

Dynamic Self-Optimization in NiFe-Layered Double Hydroxides for Alkaline Water Splitting. *Energy Environ. Sci.* **2019**, *12*, 572−581.
(17) Wu, Y.; Li, G. D.; Liu, Y.; Yang, L.; Lian, X.; Asefa, T.; Zou, X. Overall water splitting catalyzed efficiently by an ultrathin nanosheet-built, hollow Ni_3S_2-based electrocatalyst. *Adv. Funct. Mater.* **2016**, *26*, 4839−4847.
(18) Hou, Y.; Lohe, M. R.; Zhang, J.; Liu, S.; Zhuang, X.; Feng, X. Vertically Oriented Cobalt Selenide/NiFe Layered-Double-Hydroxide Nanosheets Supported on Exfoliated Graphene Foil: An Efficient 3D Electrode for Overall Water Splitting. *Energy Environ. Sci.* **2016**, *9*, 478−483.
(19) Yang, R.; Zhou, Y.; Xing, Y.; Li, D.; Jiang, D.; Chen, M.; Shi, W.; Yuan, S. Synergistic Coupling of CoFe-LDH Arrays with NiFe-LDH Nanosheet for Highly Efficient Overall Water Splitting in Alkaline Media. *Appl. Catal., B* **2019**, *253*, 131−139.
(20) Yu, L.; Zhou, H.; Sun, J.; Qin, F.; Yu, F.; Bao, J.; Yu, Y.; Chen, S.; Ren, Z. Cu Nanowires Shelled with NiFe Layered Double Hydroxide Nanosheets as Bifunctional Electrocatalysts for Overall Water Splitting. *Energy Environ. Sci.* **2017**, *10*, 1820−1827.
(21) Cai, Z.; Bu, X.; Wang, P.; Ho, J. C.; Yang, J.; Wang, X. Recent Advances in Layered Double Hydroxide Electrocatalysts for the Oxygen Evolution Reaction. *J. Mater. Chem. A* **2019**, *7*, 5069−5089.
(22) Yang, L.; Xie, L.; Ge, R.; Kong, R.; Liu, Z.; Du, G.; Asiri, A. M.; Yao, Y.; Luo, Y. Core−shell NiFe-LDH@NiFe-Bi Nanoarray: In Situ Electrochemical Surface Derivation Preparation toward Efficient Water Oxidation Electrocatalysis in Near-Neutral Media. *ACS Appl. Mater. Interfaces* **2017**, *9*, 19502−19506.
(23) Yan, Z.; Sun, H.; Chen, X.; Liu, H.; Zhao, Y.; Li, H.; Xie, W.; Cheng, F.; Chen, J. Anion Insertion Enhanced Electrodeposition of Robust Metal Hydroxide/Oxide Electrodes for Oxygen Evolution. *Nat. Commun.* **2018**, *9*, No. 2373.
(24) Cai, Z.; Bu, X.; Wang, P.; Su, W.; Wei, R.; Ho, J. C.; Yang, J.; Wang, X. Simple and Cost Effective Fabrication of 3D Porous Core−Shell Ni Nanochains@NiFe Layered Double Hydroxide Nanosheet Bifunctional Electrocatalysts for Overall Water Splitting. *J. Mater. Chem. A* **2019**, *7*, 21722−21729.
(25) Lv, X.; Xiao, X.; Cao, M.; Bu, Y.; Wang, C.; Wang, M.; Shen, Y. Efficient Carbon Dots/NiFe-Layered Double Hydroxide/$BiVO_4$ Photoanodes for Photoelectrochemical Water Splitting. *Appl. Surf. Sci.* **2018**, *439*, 1065−1071.
(26) Xue, Y.; Fishman, Z. S.; Röhr, J. A.; Pan, Z.; Wang, Y.; Zhang, C.; Zheng, S.; Zhang, Y.; Hu, S. Tunable Nano-Interfaces between MnO_x and Layered Double Hydroxides Boost Oxygen Evolving Electrocatalysis. *J. Mater. Chem. A* **2018**, *6*, 21918−21926.
(27) Wu, Z.; Zou, Z.; Huang, J.; Gao, F. $NiFe_2O_4$ Nanoparticles/NiFe Layered Double-Hydroxide Nanosheet Heterostructure Array for Efficient Overall Water Splitting at Large Current Densities. *ACS Appl. Mater. Interfaces* **2018**, *10*, 26283−26292.
(28) Gao, Z. W.; Liu, J. Y.; Chen, X. M.; Zheng, X. L.; Mao, J.; Liu, H.; Ma, T.; Li, L.; Wang, W. C.; Du, X. W. Engineering NiO/NiFe LDH Intersection to Bypass Scaling Relationship for Oxygen Evolution Reaction via Dynamic Tridimensional Adsorption of Intermediates. *Adv. Mater.* **2019**, *31*, No. 1804769.
(29) Zhang, L.; Zhang, R.; Ge, R.; Ren, X.; Hao, S.; Xie, F.; Qu, F.; Liu, Z.; Du, G.; Asiri, A. M.; et al. Facilitating Active Species Generation by Amorphous NiFe-Bi Layer Formation on NiFe-LDH Nanoarray for Efficient Electrocatalytic Oxygen Evolution at Alkaline pH. *Chem. - Eur. J.* **2017**, *23*, 11499−11503.
(30) Gao, X.; Long, X.; Yu, H.; Pan, X.; Yi, Z. Ni Nanoparticles Decorated NiFe Layered Double Hydroxide as Bifunctional Electrochemical Catalyst. *J. Electrochem. Soc.* **2017**, *164*, H307−H310.
(31) Asnavandi, M.; Yin, Y.; Li, Y.; Sun, C.; Zhao, C. Promoting Oxygen Evolution Reactions through Introduction of Oxygen Vacancies to Benchmark NiFe−OOH Catalysts. *ACS Energy Lett.* **2018**, *3*, 1515−1520.
(32) Wang, Y.; Qiao, M.; Li, Y.; Wang, S. Tuning Surface Electronic Configuration of NiFe LDHs Nanosheets by Introducing Cation Vacancies (Fe or Ni) as Highly Efficient Electrocatalysts for Oxygen Evolution Reaction. *Small* **2018**, *14*, No. 1800136.
(33) Zhou, D.; Xiong, X.; Cai, Z.; Han, N.; Jia, Y.; Xie, Q.; Duan, X.; Xie, T.; Zheng, X.; Sun, X.; Duan, X. Flame-engraved Nickel−iron Layered Double Hydroxide Nanosheets for Boosting Oxygen Evolution Reactivity. *Small Methods* **2018**, *2*, No. 1800083.
(34) Shao, M.; Ning, F.; Wei, M.; Evans, D. G.; Duan, X. Hierarchical Nanowire Arrays Based on ZnO Core−layered Double Hydroxide Shell for Largely Enhanced Photoelectrochemical Water Splitting. *Adv. Funct. Mater.* **2014**, *24*, 580−586.
(35) Cox, C. R.; Lee, J. Z.; Nocera, D. G.; Buonassisi, T. Ten-Percent Solar-to-Fuel Conversion with Nonprecious Materials. *Proc. Natl. Acad. Sci. U.S.A.* **2014**, *111*, 14057−14061.
(36) McCrory, C. C.; Jung, S.; Ferrer, I. M.; Chatman, S. M.; Peters, J. C.; Jaramillo, T. F. Benchmarking Hydrogen Evolving Reaction and Oxygen Evolving Reaction Electrocatalysts for Solar Water Splitting Devices. *J. Am. Chem. Soc.* **2015**, *137*, 4347−4357.
(37) Chen, T.; Zhang, R.; Chen, G.; Huang, J.; Chen, W.; Wang, X.; Chen, D.; Li, C.; Ostrikov, K. K. Plasma-Doping-Enhanced Overall Water Splitting: Case Study of NiCo Hydroxide Electrocatalyst. *Catal. Today* **2019**, *337*, 147−154.
(38) Anantharaj, S.; Karthick, K.; Venkatesh, M.; Simha, T. V.; Salunke, A. S.; Ma, L.; Liang, H.; Kundu, S. Enhancing Electrocatalytic Total Water Splitting at Few Layer Pt-NiFe Layered Double Hydroxide Interfaces. *Nano Energy* **2017**, *39*, 30−43.
(39) Suntivich, J.; May, K. J.; Gasteiger, H. A.; Goodenough, J. B.; Shao-Horn, Y. A Perovskite Oxide Optimized for Oxygen Evolution Catalysis from Molecular Orbital Principles. *Science* **2011**, *334*, 1383−1385.
(40) Zhao, Y.; Jia, X.; Chen, G.; Shang, L.; Waterhouse, G. I.; Wu, L.-Z.; Tung, C.-H.; O'Hare, D.; Zhang, T. Ultrafine NiO Nanosheets Stabilized by TiO_2 from Monolayer NiTi-LDH Precursors: An Active Water Oxidation Electrocatalyst. *J. Am. Chem. Soc.* **2016**, *138*, 6517−6524.
(41) Wang, X.; Yang, Y.; Diao, L.; Tang, Y.; He, F.; Liu, E.; He, C.; Shi, C.; Li, J.; Sha, J.; et al. CeO_x-Decorated NiFe-Layered Double Hydroxide for Efficient Alkaline Hydrogen Evolution by Oxygen Vacancy Engineering. *ACS Appl. Mater. Interfaces* **2018**, *10*, 35145−35153.
(42) Zhuang, L.; Ge, L.; Yang, Y.; Li, M.; Jia, Y.; Yao, X.; Zhu, Z. Ultra thin Iron-cobalt Oxide Nanosheets with Abundant Oxygen Vacancies for the Oxygen Evolution Reaction. *Adv. Mater.* **2017**, *29*, No. 1606793.
(43) Xu, W.; Lyu, F.; Bai, Y.; Gao, A.; Feng, J.; Cai, Z.; Yin, Y. Porous Cobalt Oxide Nanoplates Enriched with Oxygen Vacancies for Oxygen Evolution Reaction. *Nano Energy* **2018**, *43*, 110−116.
(44) Xu, L.; Jiang, Q.; Xiao, Z.; Li, X.; Huo, J.; Wang, S.; Dai, L. Plasma-Engraved Co_3O_4 Nanosheets with Oxygen Vacancies and High Surface Area for the Oxygen Evolution Reaction. *Angew. Chem., Int. Ed.* **2016**, *55*, 5277−5281.
(45) Bao, J.; Zhang, X.; Fan, B.; Zhang, J.; Zhou, M.; Yang, W.; Hu, X.; Wang, H.; Pan, B.; Xie, Y. Ultrathin Spinel-Structured Nanosheets Rich in Oxygen Deficiencies for Enhanced Electrocatalytic Water Oxidation. *Angew. Chem., Int. Ed.* **2015**, *54*, 7399−7404.
(46) Wang, Y.; Zhang, Y.; Liu, Z.; Xie, C.; Feng, S.; Liu, D.; Shao, M.; Wang, S. Layered Double Hydroxide Nanosheets with Multiple Vacancies Obtained by Dry Exfoliation as Highly Efficient Oxygen Evolution Electrocatalysts. *Angew. Chem., Int. Ed.* **2017**, *56*, 5867−5871.
(47) Hall, D. S. *An Electrochemical and Spectroscopic Investigation of Nickel Electrodes in Alkaline Media for Applications in Electro-catalysis*; University of Ottawa, 2014.
(48) Hanesch, M. Raman Spectroscopy of Iron Oxides and (Oxy) Hydroxides at Low Laser Power and Possible Applications in Environmental Magnetic Studies. *Geophys. J. Int.* **2009**, *177*, 941−948.
(49) Yeo, B. S.; Bell, A. T. In Situ Raman Study of Nickel Oxide and Gold-Supported Nickel Oxide Catalysts for the Electrochemical Evolution of Oxygen. *J. Phys. Chem. C* **2012**, *116*, 8394−8400.
(50) Klaus, S.; Cai, Y.; Louie, M. W.; Trotochaud, L.; Bell, A. T. Effects of Fe Electrolyte Impurities on $Ni(OH)_2$/NiOOH Structure

https://dx.doi.org/10.1021/acsami.0c11847
ACS Appl. Mater. Interfaces 2020, 12, 42850−42858

and Oxygen Evolution Activity. *J. Phys. Chem. C* **2015**, *119*, 7243−7254.
(51) Nandanapalli, K. R.; Mudusu, D. Surface Passivated Zinc Oxide (ZnO) Nanorods by Atomic Layer Deposition of Ultrathin ZnO Layers for Energy Device Applications. *ACS Appl. Nano Mater.* **2018**, *1*, 4083−4091.

https://dx.doi.org/10.1021/acsami.0c11847
ACS Appl. Mater. Interfaces 2020, 12, 42850−42858

Supporting Information

NiFe-Layered Double Hydroxide Synchronously Activated by Heterojunctions and Vacancies for the Oxygen Evolution Reaction

Yang Luo[a,b,c], Yinghong Wu[b,c,d], Donghai Wu[e], Chao Huang[a], Dezhi Xiao[a], Houyang Chen[f,*], Shili Zheng[c,*], and Paul K. Chu[a,*]

[a] *Department of Physics, Department of Materials Science and Engineering, and Department of Biomedical Engineering, City University of Hong Kong, Kowloon 999077, Hong Kong, China*

[b] *Centre for Environmental Engineering Research, Department of Civil Engineering and Department of Mechanical Engineering, The University of Hong Kong, Pokfulam 999077, Hong Kong SAR*

[c] *CAS Key Laboratory of Green Process and Engineering, National Engineering Laboratory for Hydrometallurgical Cleaner Production Technology, Institute of Process Engineering, Chinese Academy of Sciences, Beijing 100190, China*

[d] *School of Energy and Environment, City University of Hong Kong, Kowloon 999077, Hong Kong, China*

[e] *Henan Key Laboratory of Nanocomposites and Applications, Institute of Nanostructured Functional Materials, Huanghe Science and Technology College, Zhengzhou 450006, China*

[f] *Department of Chemical and Biological Engineering, University at Buffalo, The State University of New York, Buffalo, New York 14260-4200, United States*

*Corresponding authors: Paul K. Chu (paul.chu@cityu.edu.hk); Shili Zheng (slzheng@ipe.ac.cn); Houyang Chen (hchen23@buffalo.edu).

Table of Contents

References

1. Material Details

Iron (III) nitrate nonahydrate $Ni(NO_3)_2 \cdot 6H_2O$, nickel (II) nitrate hexahydrate $Fe(NO_3)_3 \cdot 9H_2O$, and urea $CO(NH_2)_2$ of GR grade were purchased from Sigma-Aldrich and used as received without further purification. Iridium oxide IrO_2 (99.9% metals basis, Ir ≥84.5%) and platinum on carbon Pt/C (Pt 10%) were purchased from Shanghai Aladdin Biochemical Technology Co., Ltd., China and used as received without further processing. The Ni foams (99.8%, 1 mm thick) were purchased from Lizhiyuan Battery Co., Ltd., China. All the solutions were prepared with ultrapure water.

2. Electrochemical Assessment and Material Characterization Details

The electrochemical tests were carried out using a three-electrode configuration in 1 M KOH solution on an electrochemical workstation (Model CHI 660D, Shanghai CHI Company, China). The as-prepared electrode, carbon rod, and saturated calomel electrode (SCE) were the working electrode, counter electrode, and reference electrode, respectively. The actual electrolytic area where the working electrode contacted the electrolyte was 1 × 1 cm^2. Linear scan voltammetry (LSV) was performed at a scanning rate of 5 mV s^{-1} after 20 cycles of cyclic voltammetry (CV) activation at 100 mV s^{-1} and the standard hydrogen electrode (RHE) calibration of SCE was performed based on the equation: E (RHE) = E (SCE) + 1.036 V. The OER overpotentials of Ni/LDH and Ni/LDH-ZnO at 10 mA cm^{-2} were determined by the LSV reverse scan method[1-3] to eliminate interferences from the oxidation peaks and the detailed procedures are described in the following. All the potentials in the polarization curves were iR_s corrected and R_s was the internal resistance obtained from the Nyquist plot. Electrochemical impedance spectroscopy (EIS) was conducted at a potential of 300 mV with an AC perturbation of 10 mV between 10^5 and 10^{-1} Hz. The Faradic efficiency was measured at 10 mA cm^{-2} for 60 min. The stability of the single electrode was evaluated by cyclic CV at 200 mV s^{-1} for 2000 cycles and that of the two-electrode configuration in overall water splitting was assessed by chronopotentiometry at 1.62 V. The Faradic efficiency was measured at 10 mA cm^{-2} for 60 min and calculated by the

H_2 (or O_2) yield (Faraday's law) determined from gas chromatography (GC, Model TRACE 1300, ThermoFisher Scientific).

The phases of the samples were identified by X-ray diffraction (XRD, Model X'pert Pro MPD, PANalytical) with Cu K_α radiation and the morphology was observed by scanning electron microscopy (SEM, Model XL30 FEG ESEM, FEI/Philips) at 10 kV and transmission electron microscopy (TEM, Model JEOL-2100F, JEOL) at 200 kV. Energy-dispersive X-ray spectroscopy (EDS, Model Genesis XM, EDAX) was carried out on the TEM for elemental mapping and X-ray photoelectron spectroscopy (XPS, ESCALAB 250Xi, Thermo Fisher) was conducted with Al K_α radiation. The electron paramagnetic resonance (EPR, Model ER200-SRC-10/12, Bruker) spectra were acquired at 9.64 GHz and room temperature and quasi-real-time Raman scattering spectroscopy was performed on the fresh electrode surfaces immediately after the electrochemical test using a laser wavelength of 633 nm (Model LabRAM HR, HORIBA). The atomic ratio of NiFe-LDH was determined by inductively-coupled plasma mass spectrometry (ICP-MS, Model iCAP Qc, Thermo Scientific).

3. DFT Calculation Details

The density-functional theory computation together with Hubbard−U (DFT + U) is carried out by adopting the Vienna Ab initio Simulation Package (VASP) code.[4] The GGA-PBE of exchange and correlation potential[5] together with the projector augmented wave (PAW) method[6] is implemented for structural relaxation. The energy cutoff for the plane-wave basis is 400 Ev and 10^{-4} eV and 0.05 eV/Å are selected for the energy change criterion and maximum force, respectively. 4.3, 3.8 and 3.4 eV are chosen for Fe, Ni and Zn[7,8] in the effective U-J terms, respectively. A >15 Å vacuum thickness is specified above the slab and the 2 × 2 × 1 k-mesh is employed for the Brillouin zone.[9]

A four electrons mechanism[10] is adopted for the oxygen evolution reactions, i.e.

$$* + H_2O = *OH + H^+ + e^- , \quad \text{(S1)}$$

$$*OH = *O + H^+ + e^- , \quad \text{(S2)}$$

$$*O + H_2O = *OOH + H^+ + e^-$$, and (S3)

$$*OOH = * + O_2 + H^+ + e^-$$, (S4)

where, the "*" indicates the active site in the OER process and "*OH", "*O", and "*OOH" refer to the intermediate species adsorbed on the active sites. The reaction free energies (ΔG_1, ΔG_2, ΔG_3, and ΔG_4) of Equations S1−S4 can be described by:

$$\Delta G = \Delta E + \Delta ZPE - T\Delta S$$, (S5)

where, ΔE, ΔZPE, and ΔS are the differences in the total energies, zero−point energies, and entropies between the final and initial states, respectively. The temperature T is 298.15 K. The zero−point energies for the OER intermediates are derived from the vibrational frequencies after structural optimization and those of free gas-phase molecules are obtained from the thermodynamic database.[11] The entropies of the intermediates located on the surface are assumed to be zero and according to previous reports[12], this approximation is reasonable. The energies of H_2O and H_2 in the gas phase (calculated from DFT) are used as references.[13] Since the electronic structure of the oxygen molecule is complicated and cannot be computed accurately by DFT, the reaction ($H_2O \rightarrow 1/2O_2 + H_2$) is employed to obtain the free energy change of oxygen molecules and it is 2.46 eV for $H_2O \rightarrow 1/2O_2 + H_2$. Hence, the equation ($G_{O2} = 4.92 - 2E_{H2} + 2E_{H2O} - (\Delta ZPE - T\Delta S)_{2H2O \rightarrow O2+2H2}$) is obtained[7,11] and the equation ($\Delta G_4 = 4.92 - \Delta G_3 - \Delta G_2 - \Delta G_1$) is deduced.[7] The overpotential η can be obtained from the Gibbs free energy differences of each step, i.e. $\eta = \max[\Delta G/e - 1.23]$.[14]

According to the previous study[7] and characterization results in this work, $Ni_2Fe_2(OH)_8$ composed of two Ni and two Fe atoms in a primitive cell is constructed (Figure S1a). One CO_3^{2-} anion and two water molecules are introduced between laminates of NiFe-LDH to balance the charge in the system[7] and taking the water environment into account.[15] According to the experimental results (section 3.1), the (110) facet of NiFe-LDH (Figure S1b) is adopted to investigate the OER mechanism. A slab model comprising four atomic layers in which the top layer is relaxed while the other layers are fixed is employed to explore the adsorption behavior of the O, OH, and OOH intermediates.

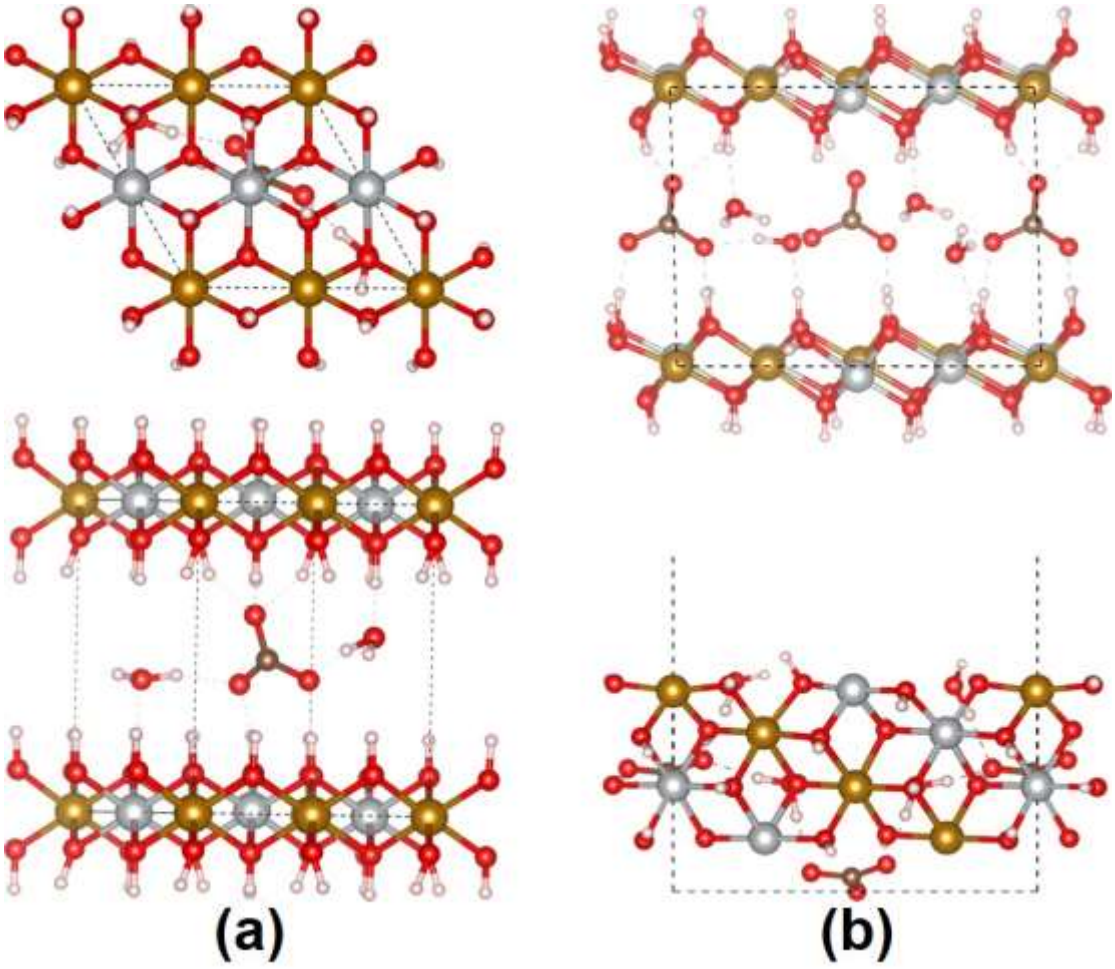

Figure S1. (a) Top (up) and side (below) views of NiFe-LDH ($Ni_2Fe_2(CO_3)(OH)_8 \cdot 2H_2O$) and (b) (110) facet (grey: nickel; gold: iron; red: oxygen; light pink: hydrogen; brown: carbon).

4. Simplification of the DFT Model

It is not straightforward to compare the results obtained by experiments and DFT calculations, especially the NiFe-LDH system. To obtain more accurate results, "Hubbard-U" and water molecules are used in the calculations. After numerous tests (more than four months using hundreds of cores of supercomputers), it is found that the DFT calculations show flaws from convergence at the ZnO-LDH heterojunction. Fundamentally, a heterojunction structure can be considered as a kind of function and therefore, the model is simplified by adopting the ZnO-doped LDH model. Nonetheless, based on the DFT technique, if one takes "Hubbard-U" and water molecules into account in the LDH model, it can only identify the properties of pure

LDH or defective LDH.[15,16] However, without "Hubbard-U" or water molecules in the model, the results become inaccurate.

5. Preparation of IrO_2 and Pt/C-Loaded Ni Foams

The IrO_2 and Pt/C loaded Ni foams were prepared by the protocol described previously.[17] Typically, 10 mg of IrO_2 or Pt/C were dissolved in 2 mL of the solution containing 0.8 mL of ultrapure water, 1.08 mL of ethyl alcohol, and 0.12 mL of 5% Nafion solution. The solution was ultrasonically treated for 30 min to form a homogeneous catalyst ink which was loaded onto the Ni foam substrate 20 times by the rotating deposition method. The amount of the materials loaded was about 5 mg cm^2.

6. LSV Reverse Scan Method

Ni/LDH-ZnO (2 min) is used as an example to illustrate the LSV reverse scan method. As shown in Figure S2, when the current density is 10 mA cm^{-2}, the potential in the backward scan is 1.44 V vs. RHE. Therefore, the overpotential at 10 mA cm^{-2} is 210 mV by subtracting 1.44 V vs. RHE from 1.23 V vs. RHE. All the OER overpotentials are thus calculated by this method to eliminate the interference of oxidation peaks.

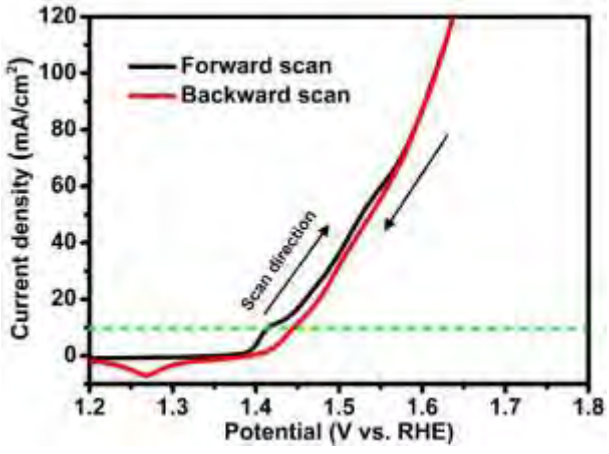

Figure S2. LSV curves showing the forward and backward scans of Ni/LDH-ZnO (2min).

7. Calculation of the Electrochemically Active Surface Area (ECSA)

The electrochemically active surface area (ECSA) is measured on the basis of measured double-layer capacitance by CV in the not apparent Faradic potential range of 0.82-0.90 V at different scanning rates of 10, 20, 30, 40, 50 and 60 mV s^{-1}. By plotting the current density difference $(j_a-j_c)/2$ at 0.86 V versus the scanning rate, the linear slope is the double layer capacitance (C_{dl}). The ECSA is calculated by dividing C_{dl} with the specific capacitance of a flat standard with a real surface area of 1 cm^2. The specific capacitance for a flat surface is normally taken to be 40 μF cm^{-2} in 1 M KOH.

8. Calculation of the Turnover Frequency (TOF)

The turnover frequency for OER is calculated by Eq. (S6):

$$\text{TOF}=\frac{\text{Number of total oxygen turnovers/cm}^2\text{ of geometric area}}{\text{Number of active sites/cm}^2\text{ of geometric area}} . \quad \text{(S6)}$$

The total number of oxygen turnovers per current density is calculated by Eq. (S7):

$$\text{No. of } O_2=(\text{per } \frac{\text{mA}}{\text{cm}^2})(\frac{1\text{ C s}^{-1}}{1000\text{ mA}})(\frac{1\text{ mol of e}}{96485.3\text{ C}})(\frac{1\text{ mol of } O_2}{4\text{ mol of e}})(\frac{6.022\times10^{23} O_2\text{ molecules}}{1\text{ mol of } O_2}) \quad \text{(S7)}$$

$$=1.56\times10^{15}\ \frac{O_2\text{ s}^{-1}}{\text{cm}^2}\ \text{per}\ \frac{\text{mA}}{\text{cm}^2}.$$

Using the assumption that either Ni or Fe acts as the active site, the active sites per real surface area can be calculated by Eq. (S8):

$$\text{Active sites per ECSA}=(\frac{2\text{ atoms/ unit cell}}{182.94\text{ Å}^3\text{/ unit cell}})^{\frac{2}{3}}=4.93\times10^{14}\text{ atoms cm}_{\text{ECSA}}^{-2} \quad \text{(S8)}$$

Finally, the plot of current densities is converted into a TOF plot according to Eq. (S9):

$$\text{TOF} = \frac{(1.56\times10^{15}\frac{O_2\text{ s}^{-1}}{\text{cm}^2}\text{ per }\frac{\text{mA}}{\text{cm}^2})\times|j|}{(\text{active sites per real surface area})\times\text{ECSA}} \quad \text{(S9)}$$

$$= \frac{(1.56\times10^{15}\frac{O_2\text{ s}^{-1}}{\text{cm}^2}\text{ per }\frac{\text{mA}}{\text{cm}^2})\times|j|}{(4.93\times10^{14}\text{ atoms per ECSA})\times\text{ECSA}}.$$

The turnover frequency for HER can also be calculated by Eq. (S6). The total number of hydrogen turnovers per current density is calculated by Eq. (S10):

$$\text{No. of } H_2 = (\text{per } \frac{\text{mA}}{\text{cm}^2})(\frac{1\text{ C s}^{-1}}{1000\text{ mA}})(\frac{1\text{ mol of e}}{96485.3\text{ C}})(\frac{1\text{ mol of } H_2}{2\text{ mol of e}})(\frac{6.022\times10^{23} O_2\text{ molecules}}{1\text{ mol of } O_2}) \quad \text{(S10)}$$

$$= 3.12\times10^{15}\ \frac{O_2\text{ s}^{-1}}{\text{cm}^2}\ \text{per}\ \frac{\text{mA}}{\text{cm}^2}.$$

Assuming that either Ni or Fe acts as the active site, the active sites per real surface area can be calculated by Eq. (S8). Finally, the plot of current densities can be converted into a TOF plot according to Eq. (S11):

$$\text{TOF} = \frac{(3.12\times10^{15}\ \frac{O_2\text{ s}^{-1}}{\text{cm}^2}\ \text{per}\ \frac{\text{mA}}{\text{cm}^2})\times|j|}{(\text{active sites per real surface area})\times\text{ECSA}} \quad \text{(S11)}$$

$$= \frac{(3.12\times10^{15}\ \frac{O_2\text{ s}^{-1}}{\text{cm}^2}\ \text{per}\ \frac{\text{mA}}{\text{cm}^2})\times|j|}{(4.93\times10^{14}\text{ atoms per ECSA})\times\text{ECSA}}.$$

9. Effects of the Ni/Fe Ratio on the Catalytic Performance of the NiFe-LDH Samples.

Table S1. Nomenclatures of the samples with different molar ratios of (Ni/Fe) introducd in the beginning.

Abbreviation	Ratios of (Ni/Fe) in the reaction
$Ni_{0.7}Fe_{0.3}$	0.7 / 0.3
$Ni_{0.6}Fe_{0.4}$	0.6 / 0.4
$Ni_{0.5}Fe_{0.5}$	0.5 / 0.5
$Ni_{0.4}Fe_{0.6}$	0.4 / 0.6
$Ni_{0.3}Fe_{0.7}$	0.3 / 0.7

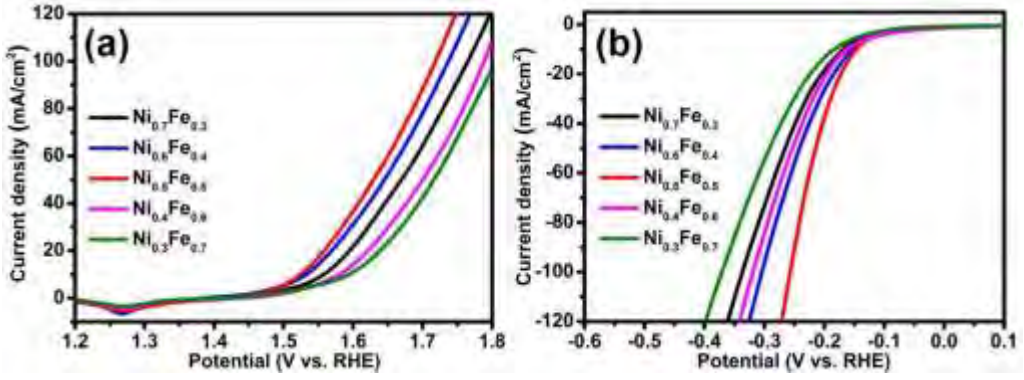

Figure S3. (a) OER polarization curves of the NiFe-LDH samples with different ratios of (Ni/Fe) and (b) HER polarization curves of the NiFe-LDH samples with different ratios of (Ni: Fe).

Table S1 and Figure S3 show that the NiFe-LDH sample with a (Ni: Fe) molar ratio of (0.5: 0.5) delivers the best OER and HER catalytic performance.

10. Supplementary Data

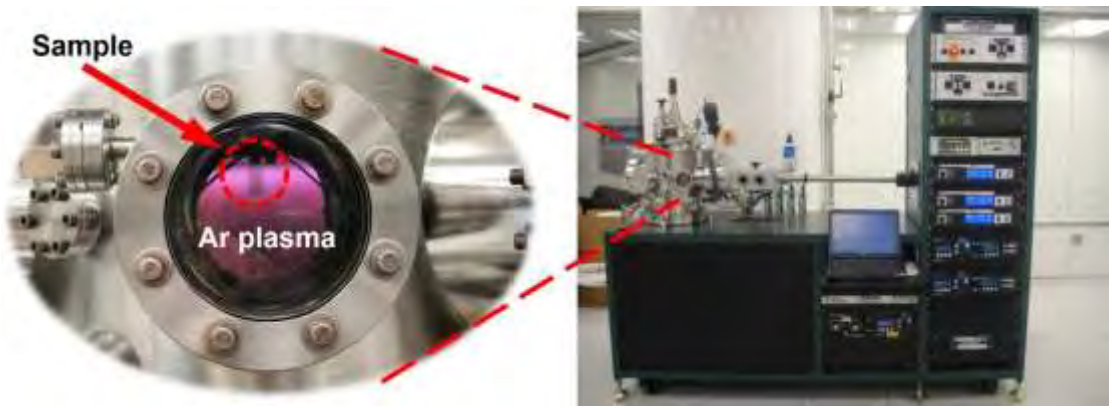

Figure S4. ATC ORION plasma magnetron sputtering system.

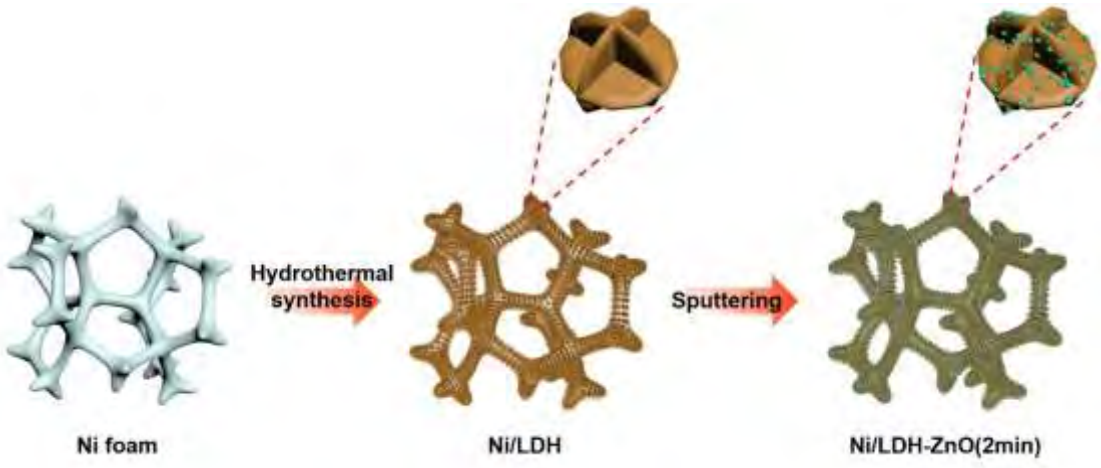

Figure S5. Schematic illustration of the fabrication process of the self-supported catalytic electrode.

Table S2. Nomenclatures of the different electrodes.

Abbreviation	Description
Ni	Nickel foam
Ni/LDH	Nickel foam loaded with hydrothermally synthesized NiFe-LDH
Ni/LDH-ZnO (1 min)	Ni/LDH after ZnO sputtering for 1 minute
Ni/LDH-ZnO (2 min)	Ni/LDH after ZnO sputtering for 2 minutes
Ni/LDH-ZnO (3 min)	Ni/LDH after ZnO sputtering for 3 minutes
Ni-LDH (2 min)	Nickel foam after ZnO sputtering for 2 minutes
Ni/IrO_2	Nickel foam loaded with commercial IrO_2
Ni/Pt/C	Nickel foam loaded with commercial Pt/C

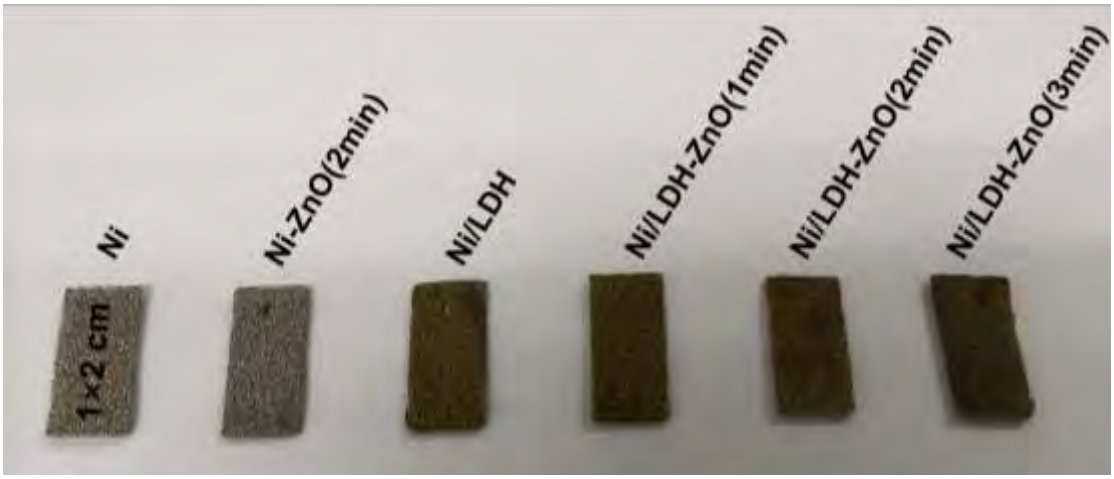

Figure S6. Photographs of the samples.

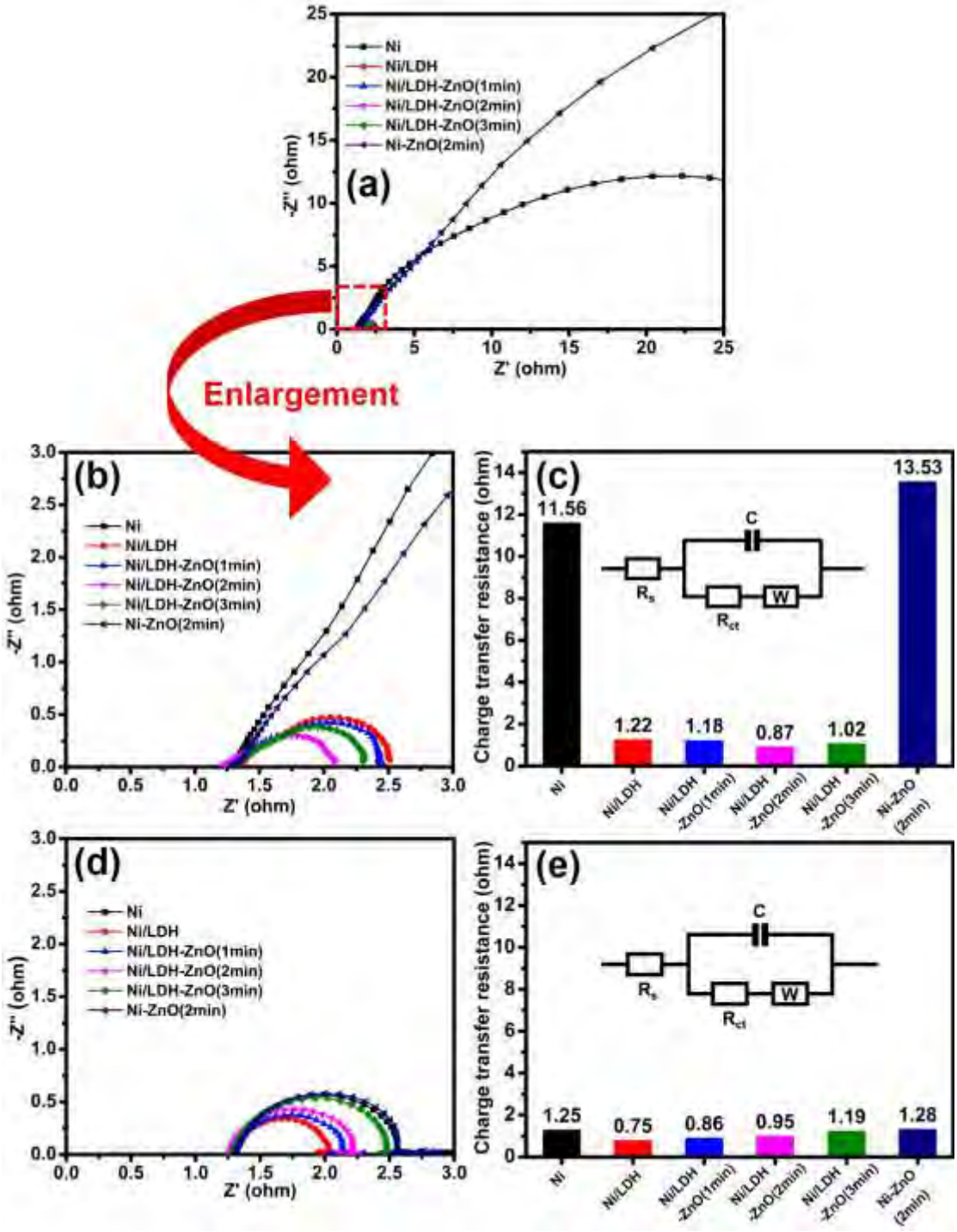

Figure S7. (a, b) Nyquist plots for OER, (c) charge-transfer resistance for OER, (d) Nyquist plots for HER, and (e) charge-transfer resistance for HER (EIS measured at an overpotential of 300 mV).

Table S3. Atomic ratios determined by ICP-MS.

Samples	Atomic ratios of Ni/Fe/Zn (normalized by Ni)
Ni/LDH	1 / 0.78 / 0
Ni/LDH-ZnO(1min)	1 / 0.78 / 0.012
Ni/LDH-ZnO(2min)	1 / 0.78 / 0.022
Ni/LDH-ZnO(3min)	1 / 0.78 / 0.034
Ni/LDH-ZnO(2min) after continuous OER for 20 h	1 / 0.76 / 0.08
Ni/LDH after continuous HER for 20 h	1 / 0.79 / 0

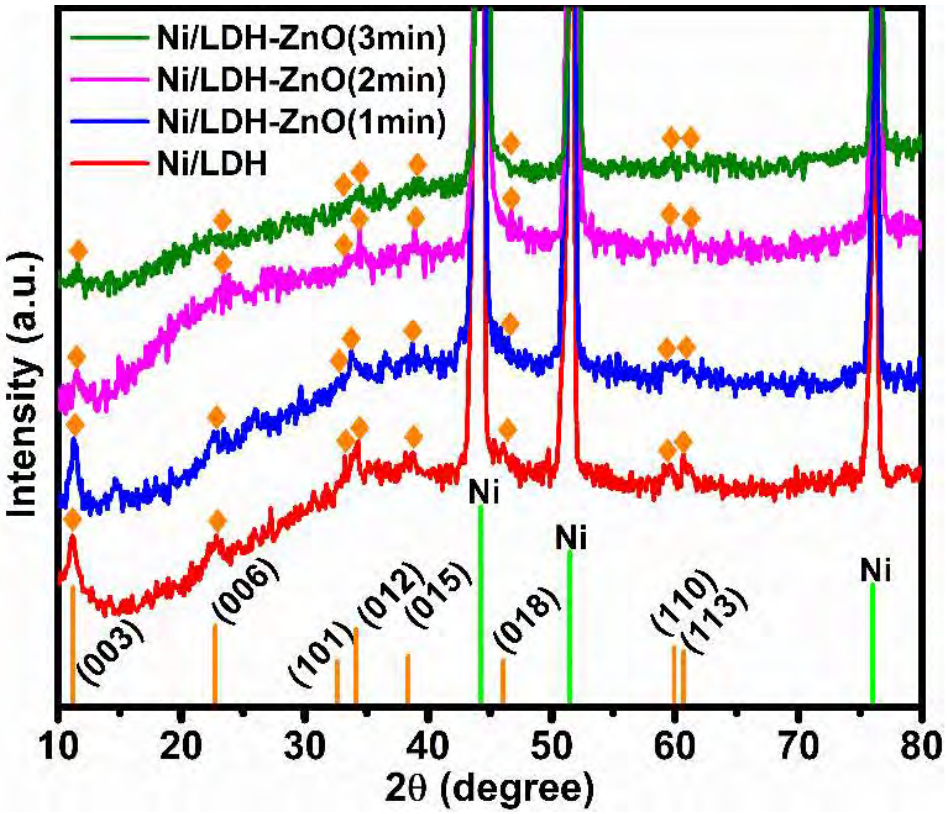

Figure S8. XRD patterns of Ni/LDH and Ni/LDH-ZnO for different deposition times.

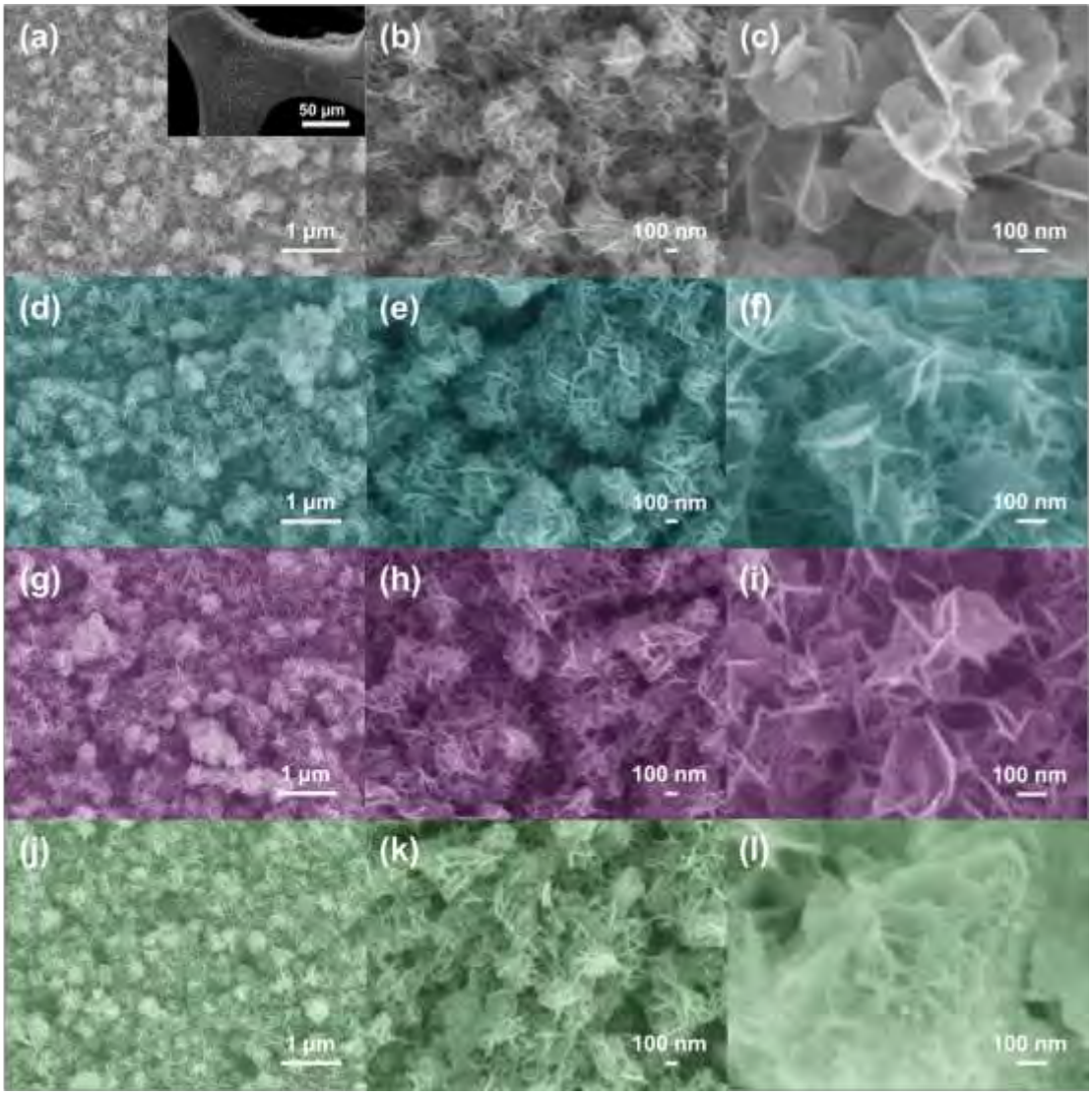

Figure S9. SEM images: (a, b, c) Ni/LDH (inset showing the uniformity of NiFe-LDH on Ni Foam at low magnification), (d, e, f) Ni/LDH-ZnO (1 min), (g, h, i) Ni/LDH-ZnO (2 min), and (j, k, l) Ni/LDH-ZnO (3 min).

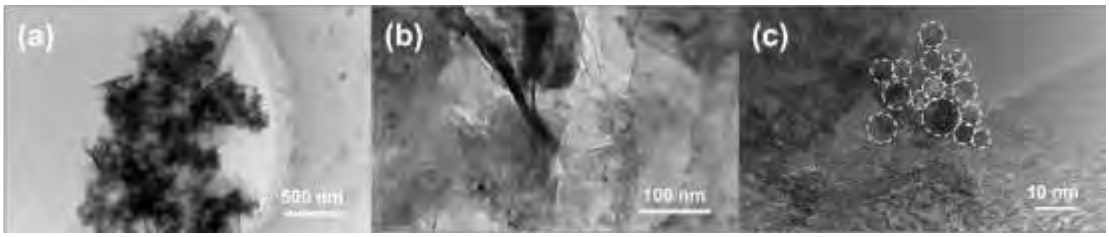

Figure S10. (a, b) TEM images and (c) HR-TEM image of Ni/LDH-ZnO for a long deposition time (10 min).

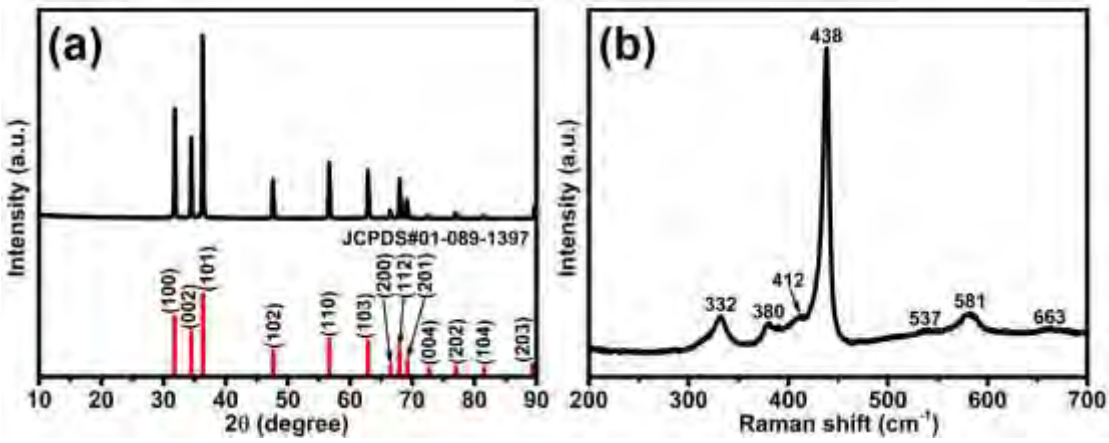

Figure S11. (a) XRD pattern and (b) Raman spectrum of Ni-ZnO (1 h).

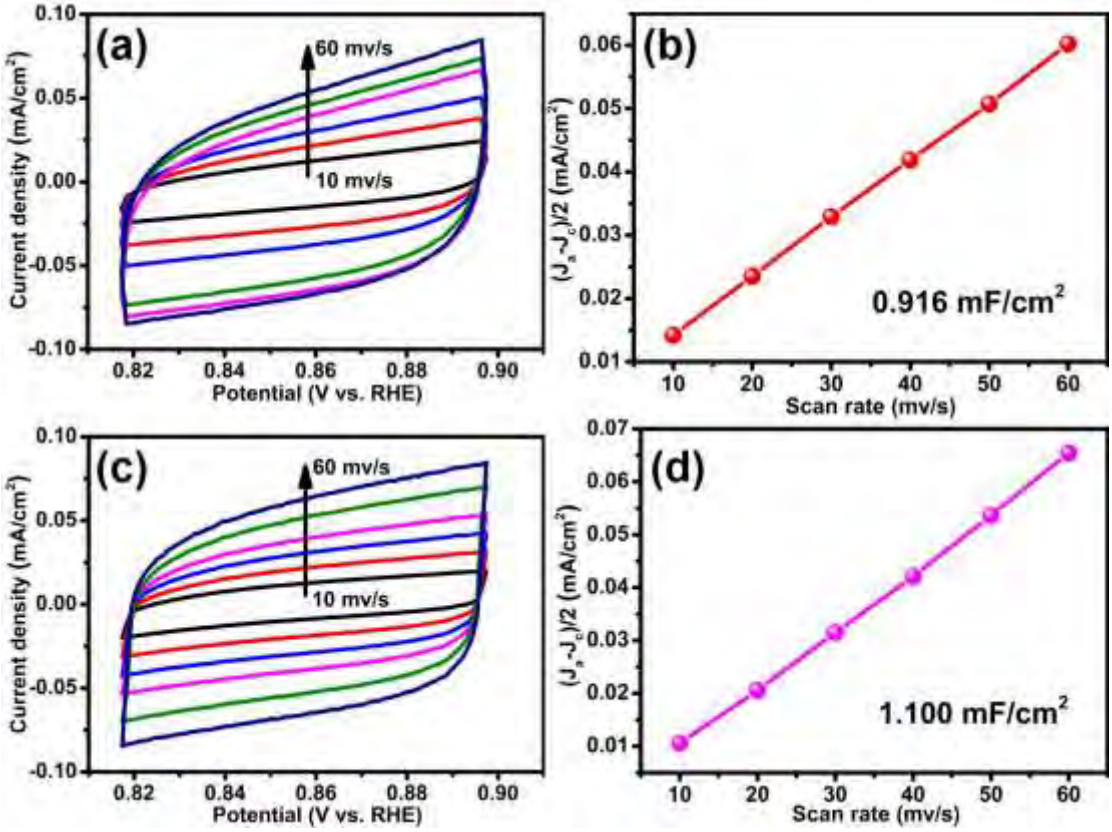

Figure S12. CV curves obtained at different scanning rates and $(j_a-j_c)/2$ at 0.86 V with respect to scanning rates: (a, b) Ni/LDH and (c, d) Ni/LDH-ZnO (2 min).

By calculating the slope from the linear relationship of $(j_a-j_c)/2$ at 0.86 V vs. scanning rate, the electrical double layer capacitances (C_{dl}) of Ni/LDH and Ni/LDH-ZnO (2 min) are calculated to be 0.916 and 1.100 mF cm^{-2}, respectively. As a result, the ECSAs of Ni/LDH and Ni/LDH-ZnO(2min) are calculated to be 22.9 and 27.5 cm^2_{ECSA}, respectively.

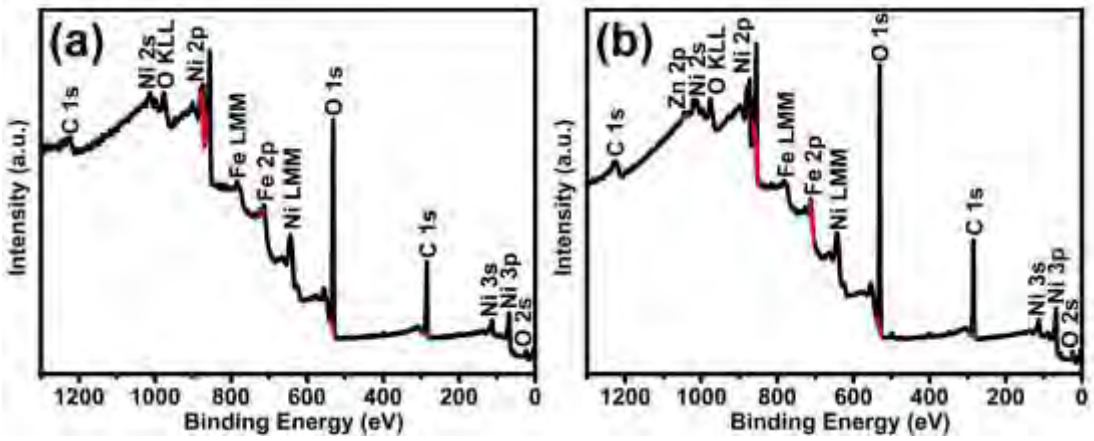

Figure S13. XPS survey spectra: (a) Ni/LDH and (b) Ni/LDH-ZnO (2 min).

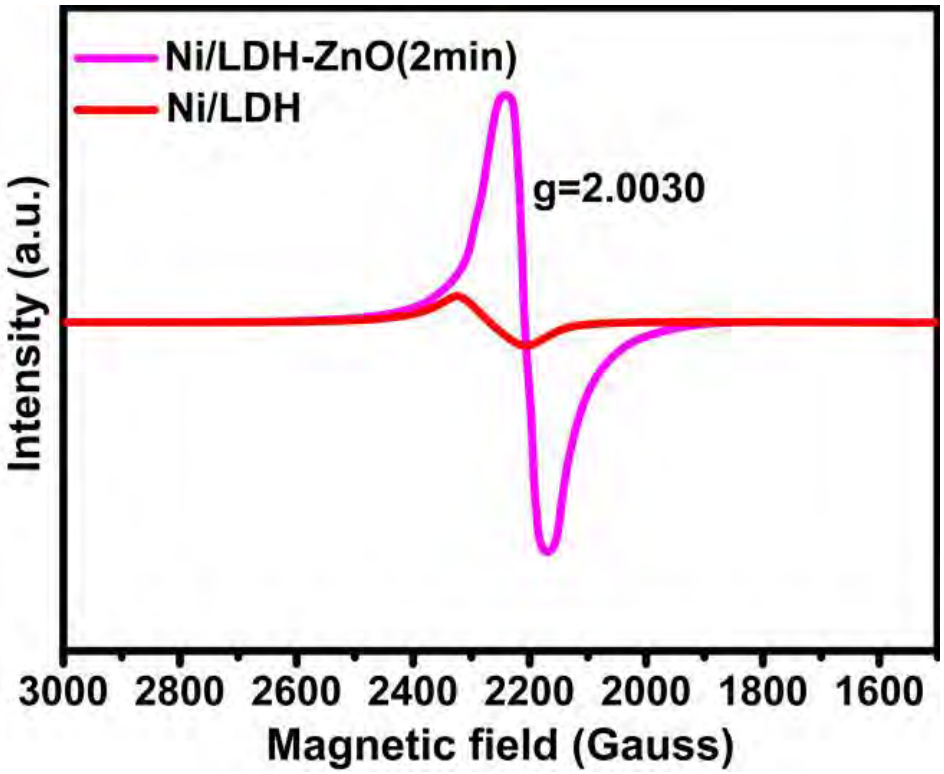

Figure S14. EPR spectra of Ni/LDH-ZnO (2 min) and Ni/LDH.

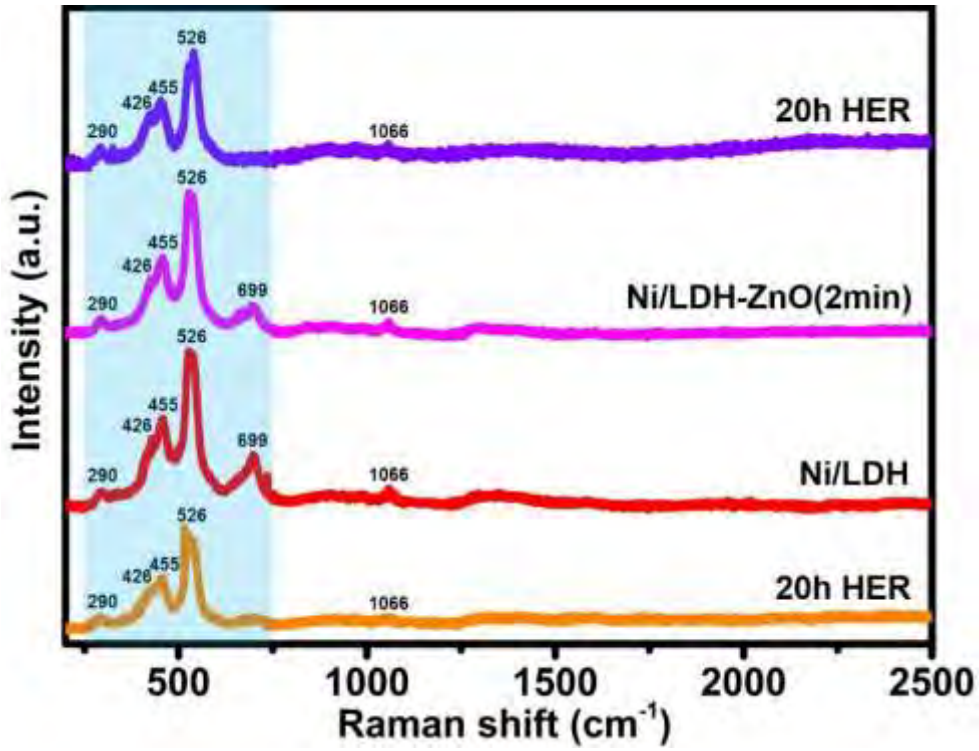

Figure S15. Quasi-real-time Raman spectra under HER conditions.

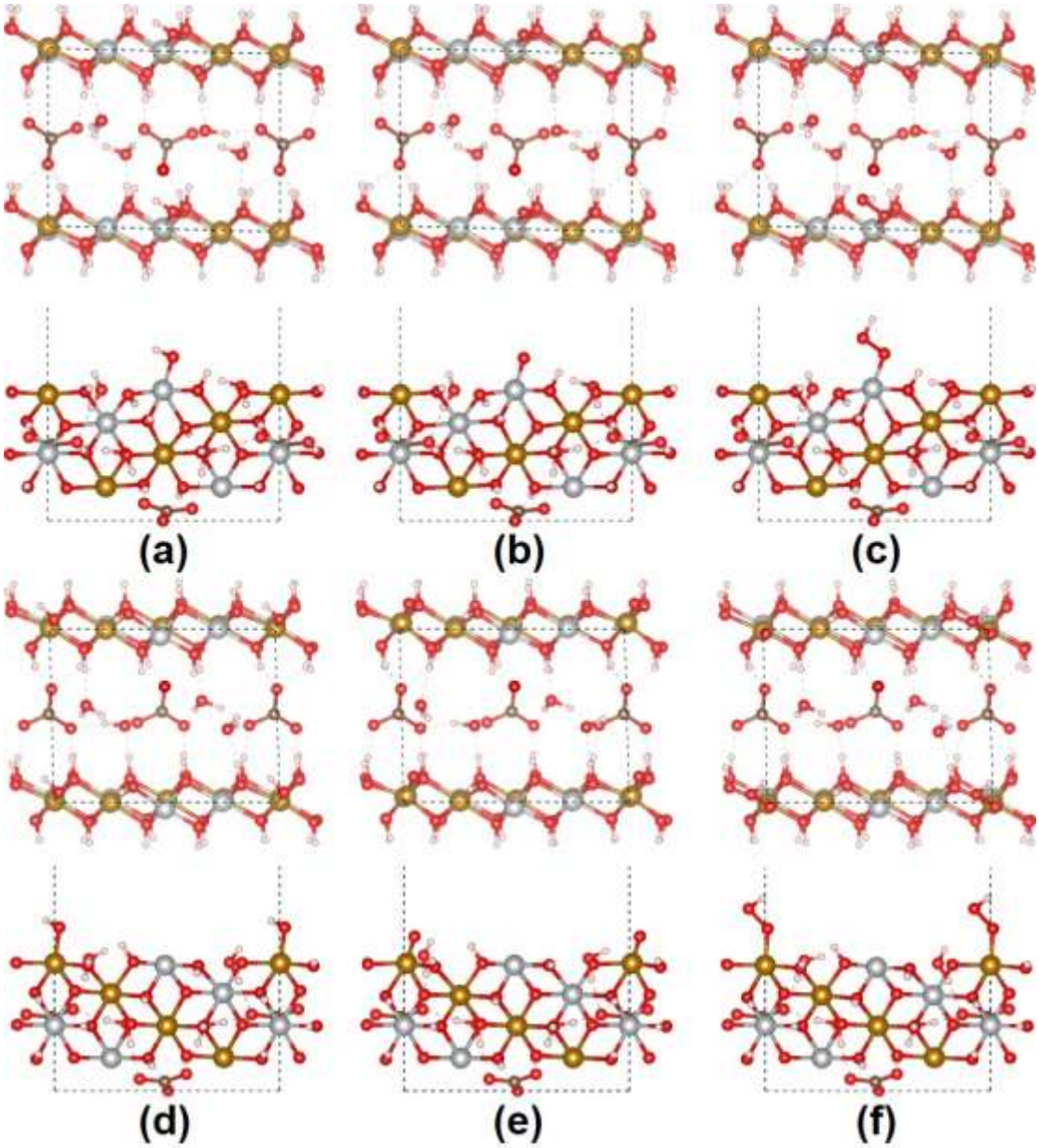

Figure S16. Top (up) and side (below) views of (a) OH, (b) O, and (c) OOH intermediates adsorbed on the Ni site of the (110) facet of NiFe-LDH, and (d) OH, (e) O, and (f) OOH intermediates adsorbed on the Fe site of the (110) facet of NiFe-LDH (grey: nickel; gold: iron; red: oxygen; light pink: hydrogen; brown: carbon).

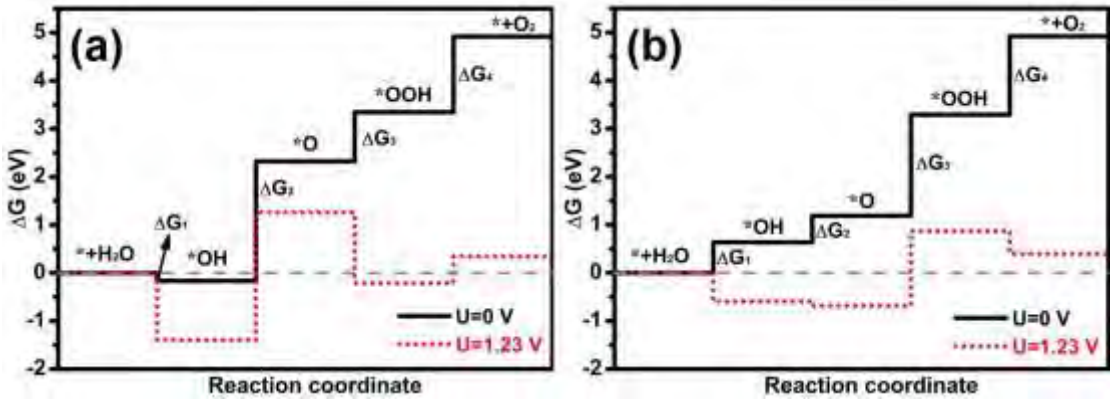

Figure S17. Free energy curves of the OER process on (a) Ni and (b) Fe sites of the (110) facet of NiFe-LDH (grey: nickel; gold: iron; red: oxygen; light pink: hydrogen; brown: carbon).

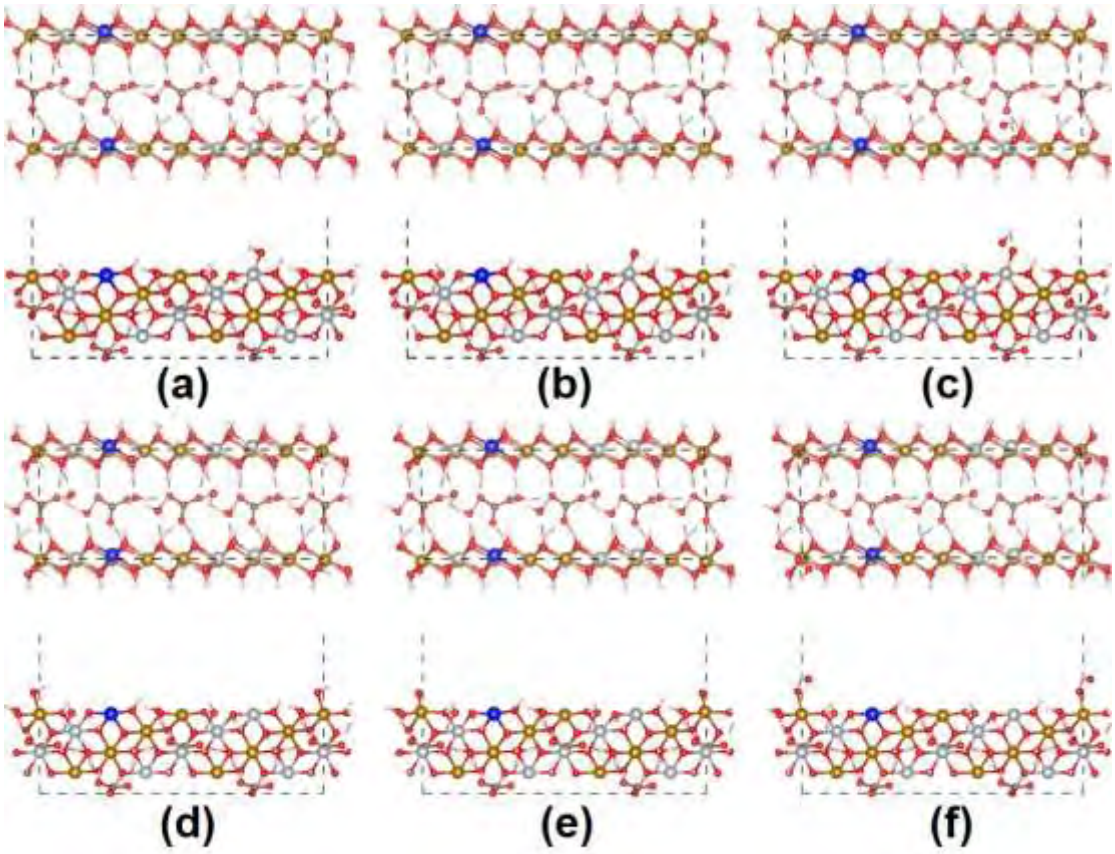

Figure S18. Top and side views of adsorption of (a) OH, (b) O, and (c) OOH intermediates at the Ni sites on the Zn-doped (110) facet of NiFe-LDH, and (d) OH, (e) O, and (f) OOH intermediates at the Fe sites on the Zn-doped (110) facet of NiFe-LDH.

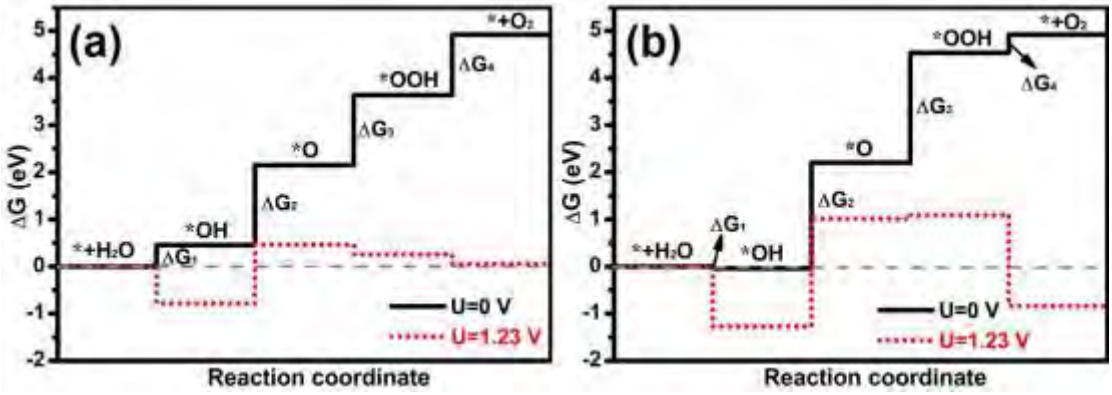

Figure S19. Free energy plots of the OER process at (a) Ni and (b) Fe sites on the Zn-doped (110) facet of NiFe-LDH.

Table S4. Amount (|e|) of electrons transferred from Ni/Fe on the pristine and Zn-doped (110) facet to other atoms.

Intermediates	Pristine (110) facet		Zn-doped (110) facet	
	Ni	Fe	Ni	Fe
OH*	0.885	1.246	1.08	1.225
O*	1.169	1.537	1.186	1.405
OOH*	0.917	1.435	1.101	1.42

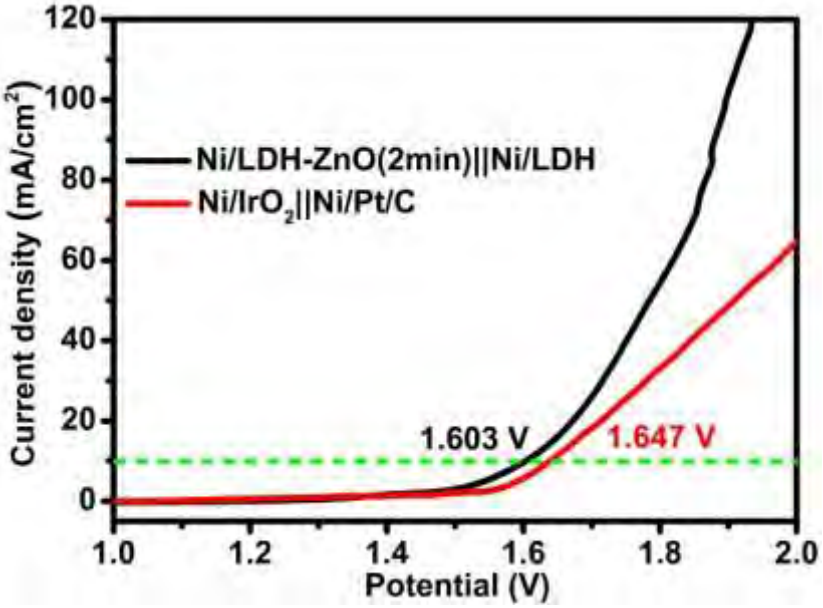

Figure S20. Comparison of the water splitting performance between the Ni/LDH-ZnO (2 min)||Ni/LDH system and the Ni/IrO_2||Ni/Pt/C system.

Table S5. Summary of the electrocatalytic performance of different electrocatalysts reported recently for overall water splitting in 1 M KOH.

Samples	η for OER at 10 mA cm^{-1} (mV)	η for HER at 10 mA cm^{-1} (mV)	Voltage for overall water splitting (V)	Refs.
Ni foam/LDH(-ZnO)	210	148	1.603	This work
Ni foam/LDH	250	148	1.678	This work
Co-Fe oxyphosphide	280	180	1.69	[18]
Co_xFe_{1-x}-P film	290	169	1.64	[19]
CoP/rGO	340	150	1.70	[20]
CoP_2/rGO	370	115	1.68	[21]
Ni foam/S:CoP	270	109	~1.60	[22]
CoP film/Cu foil	345	94	~1.69	[23]
Carbon cloth/FeP@Fe-P-O	288	120	1.69	[24]
Ni foam/$NiFe_3N$	202	75	1.62	[25]
Ni foam/V	292	176	1.74	[26]
Ni foam/VOOH	270	164	1.62	[27]
CP/CTs/Co-S	306	190	1.74	[28]
Ni foil/Ni_5P_4	290	150	1.70	[29]
Ni foam/Co-Ni-B	313	205	1.72	[30]

Ni foam/$NiCo_2O_4$	290	110	1.65	[31]
$CoP/CoP_2/Al_2O_3$	300	138	1.65	[32]
Carbon cloth/Co_4N-$VN_{1-x}O_x$	263	118	1.64	[33]
Ni foam/NiFe-LDH	210	210	1.70	[34]

ZnO deposition by plasma magnetron sputtering improves the OER properties significantly and so Ni/LDH-ZnO (2 min) serves as an outstanding anode under alkaline conditions. Furthermore, Ni/LDH without ZnO is a competitive HER catalytic electrode under alkaline conditions. Therefore, the combination of Ni/LDH-ZnO (2 min) and Ni/LDH delivers excellent performance in overall water splitting under alkaline conditions and the results surpasses those of most of state-of-the-art bifunctional catalysts as shown in Table S4. In addition, Ni/LDH is a precursor of Ni/LDH-ZnO (2 min) during preparation and the production cost can be reduced.

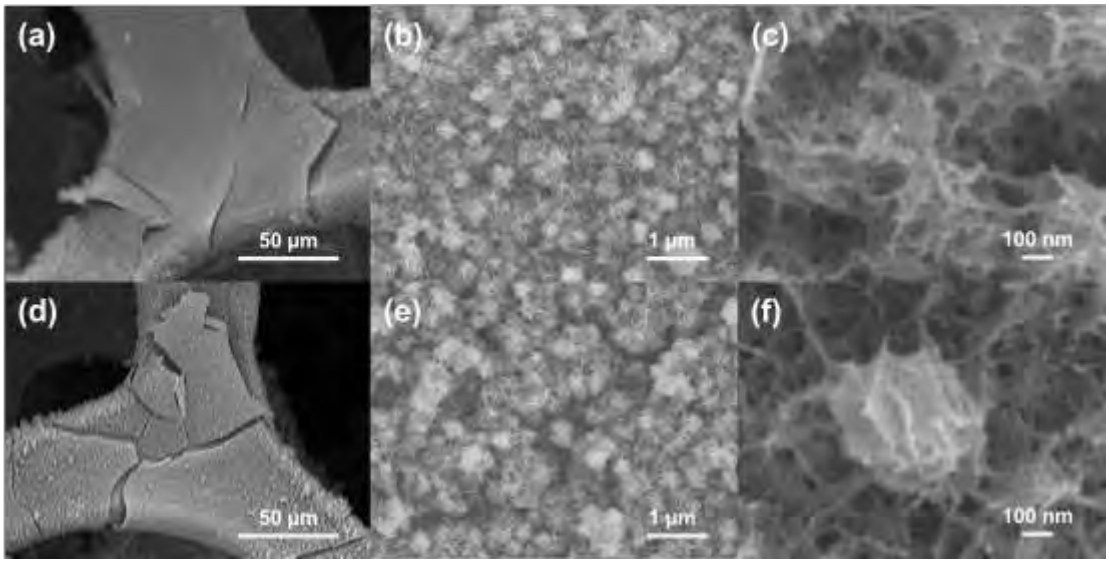

Figure S21. (a, b, c) SEM images of Ni/LDH-ZnO (2 min) after the stability test and (d, e, f) SEM images of Ni/LDH after the stability test.

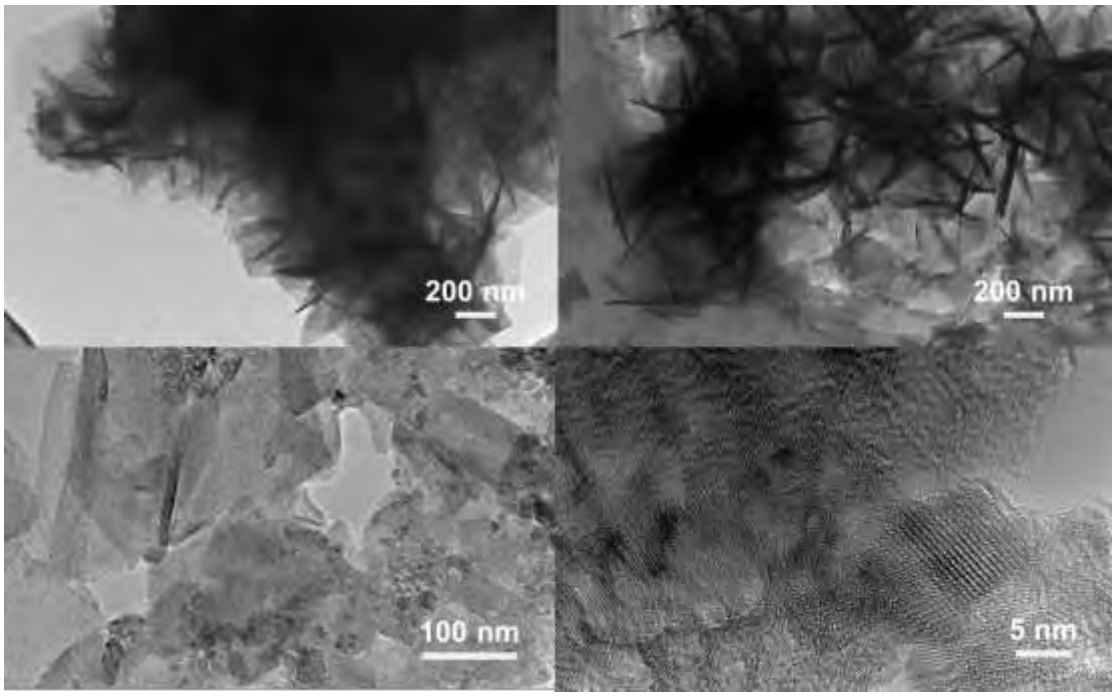

Figure S22. (a) TEM image of Ni/LDH after the stability test, (b, c) TEM images of Ni/LDH-ZnO (2 min) after the stability test, and (d) HR-TEM image of Ni/LDH-ZnO (2 min) after the stability test.

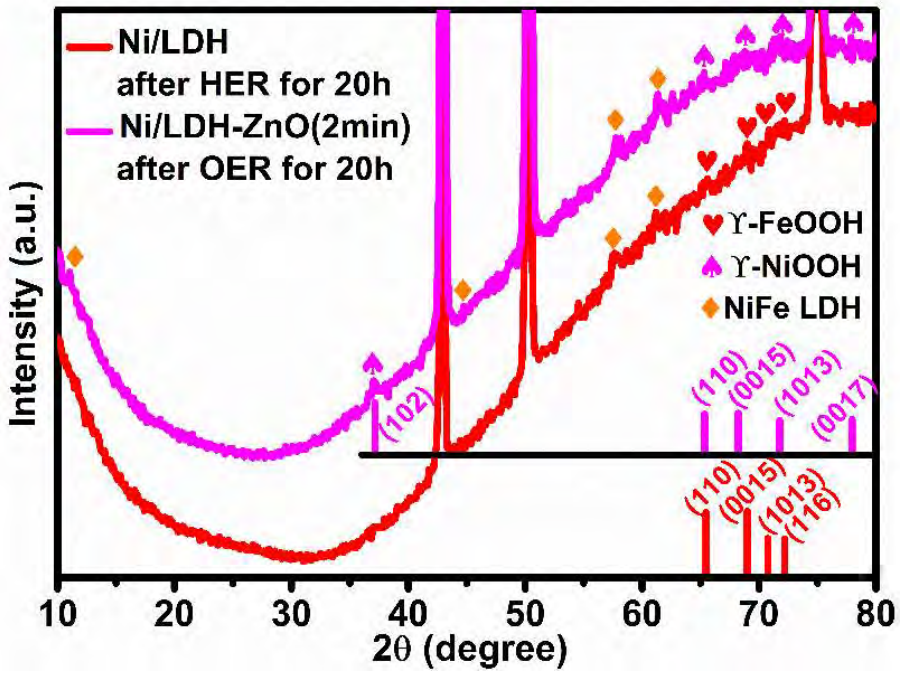

Figure S23. XRD patterns of Ni/LDH and Ni/LDH-ZnO (2 min) after the stability test.

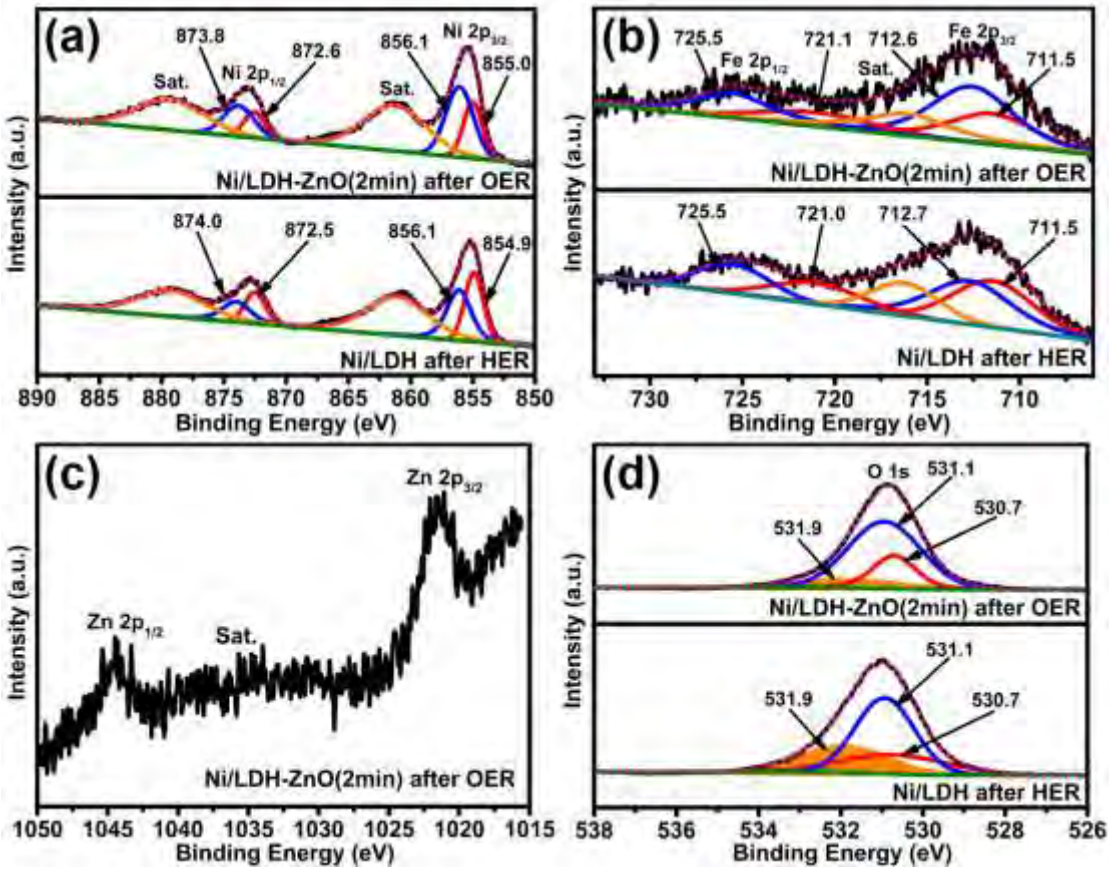

Figure S24. High-resolution XPS spectra of Ni/LDH and Ni/LDH-ZnO (2 min) after the stability test: (a) Ni 2p, (b) Fe 2p, (c) Zn 2p, and (d) O 1s.

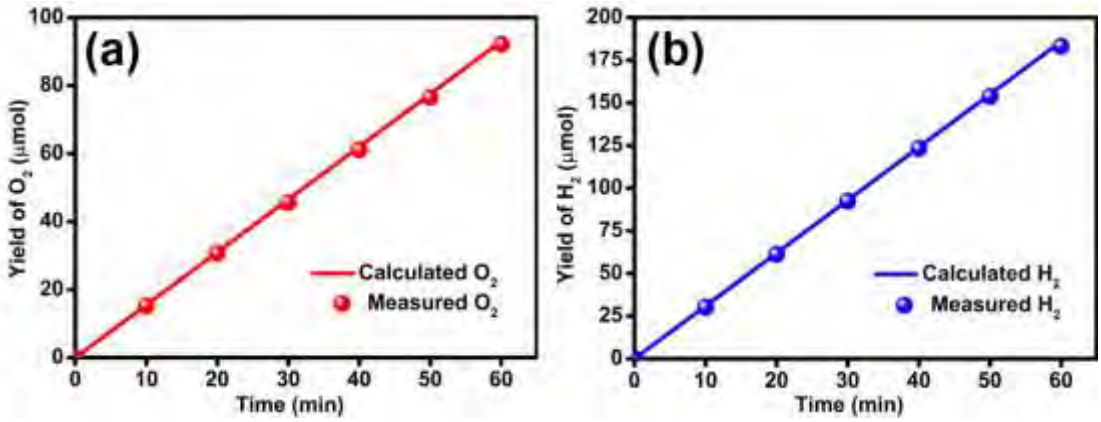

Figure S25. (a) Yield of O_2 on Ni/LDH-ZnO (2 min) and (b) yield of H_2 on Ni/LDH in overall water splitting at a current density of 10 mA cm^{-2} for 60 min.

References

(1) Yan, H.; Xie, Y.; Wu, A.; Cai, Z.; Wang, L.; Tian, C.; Zhang, X.; Fu, H., Anion-Modulated HER and OER Activities of 3D Ni−V−Based Interstitial Compound Hterojunctions for High-Efficiency and Stable Overall Water Splitting. Adv. Mater. 2019, 31, 1901174.

(2) Duan, J.; Chen, S.; Zhao, C., Ultrathin Metal-Organic Framework Array for Efficient Electrocatalytic Water Splitting. Nat. Commun. 2017, 8, 15341.

(3) You, B.; Jiang, N.; Sheng, M. L.; Bhushan, M. W.; Sun, Y. T., Hierarchically Porous Urchin-Like Ni_2P Superstructures Supported on Nickel Foam as Efficient Bifunctional Electrocatalysts for Overall Water Splitting. ACS catal. 2016, 6, 714.

(4) Kresse, G.; Furthmüller, J., Software VASP, Vienna (1999). Phys. Rev. B 1996, 54, 169.

(5) Perdew, J. P.; Burke, K.; Ernzerhof, M., Generalized Gradient Approximation Made Simple. Phys. Rev. Lett. 1996, 77, 3865.

(6) Blöchl, P. E., Projector Augmented-Wave Method. Phys. Rev. B 1994, 50, 17953.

(7) Bi, Y.; Cai, Z.; Zhou, D.; Tian, Y.; Kuang, Y.; Li, Y.; Sun, X.; Duan, X., Understanding the Incorporating Effect of Co^{2+}/Co^{3+} in NiFe-Layered Double Hydroxide for Electrocatalytic Oxygen Evolution Reaction. J. Catal. 2018, 358, 100-107.

(8) Paudel, T. R.; Lambrecht, W. R., First-Principles Calculation of the O Vacancy in ZnO: A Self-Consistent Gap-Corrected Approach. Phys. Rev. B 2008, 77, 205202.

(9) Monkhorst, H. J.; Pack, J. D., Special Points for Brillouin-Zone Integrations. Phys. Rev. B 1976, 13, 5188.

(10) Skúlason, E.; Tripkovic, V.; Björketun, M. E.; Gudmundsdottir, S.; Karlberg, G.; Rossmeisl, J.; Bligaard, T.; Jónsson, H.; Nørskov, J. K., Modeling the Electrochemical Hydrogen Oxidation and Evolution Reactions on the Basis of Density Functional Theory Calculations. J. Phys. Chem. C 2010, 114, 18182-18197.

(11) Lin, S.; Ye, X.; Gao, X.; Huang, J., Mechanistic Insight into the Water Photooxidation on Pure and Sulfur-Doped g-C_3N_4 Photocatalysts from DFT Calculations with Dispersion Corrections. J. Mol. Catal. A: Chem. 2015, 406, 137-144.
(12) Rossmeisl, J.; Logadottir, A.; Nørskov, J. K., Electrolysis of Water on (Oxidized) Metal Surfaces. Chem. Phys. 2005, 319, 178-184.
(13) Nørskov, J. K.; Rossmeisl, J.; Logadottir, A.; Lindqvist, L.; Kitchin, J. R.; Bligaard, T.; Jonsson, H., Origin of the Overpotential for Oxygen Reduction at a Fuel-Cell Cathode. J. Phys. Chem. B 2004, 108, 17886-17892.
(14) Fei, H.; Dong, J.; Feng, Y.; Allen, C. S.; Wan, C.; Volosskiy, B.; Li, M.; Zhao, Z.; Wang, Y.; Sun, H., General Synthesis and Definitive Structural Identification of MN_4C_4 Single-Atom Catalysts with Tunable Electrocatalytic Activities. Nat. Catal. 2018, 1, 63-72.
(15) Zhang, J.; Liu, J.; Xi, L.; Yu, Y.; Chen, N.; Sun, S.; Wang, W.; Lange, K. M.; Zhang, B., Single-Atom Au/NiFe Layered Double Hydroxide Electrocatalyst: Probing the Origin of Activity for Oxygen Evolution Reaction. J. Am. Chem. Soc. 2018, 140, 3876-3879.
(16) Wang, Y.; Qiao, M.; Li, Y.; Wang, S., Tuning Surface Electronic Configuration of NiFe LDHs Nanosheets by Introducing Cation Vacancies (Fe or Ni) as Highly Efficient Electrocatalysts for Oxygen Evolution Reaction. Small 2018, 14, 1800136.
(17) Xing, J.; Li, H.; Cheng, M. M.-C.; Geyer, S. M.; Ng, K. S., Electro-synthesis of 3D Porous Hierarchical Ni–Fe Phosphate Film/Ni Foam as a High-Efficiency Bifunctional Electrocatalyst for Overall Water Splitting. J. Mater. Chem. A 2016, 4, 13866-13873.
(18) Zhang, P.; Lu, X. F.; Nai, J.; Zang, S. Q.; Lou, X. W., Construction of Hierarchical Co–Fe Oxyphosphide Microtubes for Electrocatalytic Overall Water Splitting. Adv. Sci 2019, 6, 1900576.
(19) Yoon, S.; Kim, J.; Lim, J.-H.; Yoo, B., Cobalt Iron-Phosphorus Synthesized by Electrodeposition as Highly Active and Stable Bifunctional Catalyst for Full Water Splitting. J. Electrochem. Soc. 2018, 165, H271.

(20) Jiao, L.; Zhou, Y.-X.; Jiang, H.-L., Metal–Organic Framework-Based CoP/Reduced Graphene Oxide: High-Performance Bifunctional Electrocatalyst for Overall Water Splitting. Chem. Sci. 2016, 7, 1690-1695.

(21) Wang, J.; Yang, W.; Liu, J., CoP_2 Nanoparticles on Reduced Graphene Oxide Sheets as a Super-Efficient Bifunctional Electrocatalyst for Full Water Splitting. J. Mater. Chem. A 2016, 4, 4686-4690.

(22) Anjum, M. A. R.; Okyay, M. S.; Kim, M.; Lee, M. H.; Park, N.; Lee, J. S., Bifunctional Sulfur-Doped Cobalt Phosphide Electrocatalyst Outperforms All-Noble-Metal Electrocatalysts in Alkaline Electrolyzer for Overall Water Splitting. Nano Energy 2018, 53, 286-295.

(23) Jiang, N.; You, B.; Sheng, M.; Sun, Y., Electrodeposited Cobalt-Phosphorous-Derived Films as Competent Bifunctional Catalysts for Overall Water Splitting. Angew. Chem., Int. Ed. 2015, 54, 6251-6254.

(24) Yan, Y.; Xia, B. Y.; Ge, X.; Liu, Z.; Fisher, A.; Wang, X., A Flexible Electrode Based on Iron Phosphide Nanotubes for Overall Water Splitting. Chem. - Eur. J. 2015, 21, 18062-18067.

(25) Zhang, B.; Xiao, C.; Xie, S.; Liang, J.; Chen, X.; Tang, Y., Iron–Nickel Nitride Nanostructures In Situ Grown on Surface-Redox-Etching Nickel Foam: Efficient and Ultrasustainable Electrocatalysts for Overall Water Splitting. Chem. Mater. 2016, 28, 6934-6941.

(26) Yu, Y.; Li, P.; Wang, X.; Gao, W.; Shen, Z.; Zhu, Y.; Yang, S.; Song, W.; Ding, K., Vanadium Nanobelts Coated Nickel Foam 3D Bifunctional Electrode with Excellent Catalytic Activity and Stability for Water Electrolysis. Nanoscale 2016, 8, 10731-10738.

(27) Shi, H.; Liang, H.; Ming, F.; Wang, Z., Efficient Overall Water-Splitting Electrocatalysis Using Lepidocrocite VOOH Hollow Nanospheres. Angew. Chem., Int. Ed. 2017, 56, 573-577.

(28) Wang, J.; Zhong, H.-x.; Wang, Z.-l.; Meng, F.-l.; Zhang, X.-b., Integrated Three-Dimensional Carbon Paper/Carbon Tubes/Cobalt-Sulfide Sheets as an Efficient Electrode for Overall Water Splitting. ACS Nano 2016, 10, 2342-2348.

(29) Ledendecker, M.; Krick Calderón, S.; Papp, C.; Steinrück, H. P.; Antonietti, M.; Shalom, M., The Synthesis of Nanostructured Ni_5P_4 Films and Their Use as a Non-noble Bifunctional Electrocatalyst for Full Water Splitting. Angew. Chem., Int. Ed. 2015, 54, 12361-12365.

(30) Xu, N.; Cao, G.; Chen, Z.; Kang, Q.; Dai, H.; Wang, P., Cobalt Nickel Boride as an Active Electrocatalyst for Water Splitting. J. Mater. Chem. A 2017, 5, 12379-12384.

(31) Gao, X.; Zhang, H.; Li, Q.; Yu, X.; Hong, Z.; Zhang, X.; Liang, C.; Lin, Z., Hierarchical $NiCo_2O_4$ Hollow Microcuboids as Bifunctional Electrocatalysts for Overall Water-Splitting. Angew. Chem., Int. Ed. 2016, 55, 6290-6294.

(32) Li, W.; Zhang, S.; Fan, Q.; Zhang, F.; Xu, S., Hierarchically Scaffolded CoP/CoP_2 Nanoparticles: Controllable Synthesis and Their Application as a Well-Matched Bifunctional Electrocatalyst for Overall Water Splitting. Nanoscale 2017, 9, 5677-5685.

(33) Dutta, S.; Indra, A.; Feng, Y.; Han, H.; Song, T., Promoting Electrocatalytic Overall Water Splitting with Nanohybrid of Transition Metal Nitride-Oxynitride. Appl. Catal., B 2019, 241, 521-527.

(34) Luo, J.; Im, J.-H.; Mayer, M. T.; Schreier, M.; Nazeeruddin, M. K.; Park, N.-G.; Tilley, S. D.; Fan, H. J.; Grätzel, M., Water Photolysis at
12.3% Efficiency via Perovskite Photovoltaics and Earth-Abundant Catalysts. Science 2014, 345, 1593-1596.